AD A286 097

Solid State Research

94-34649

1994:2

Lincoln Laboratory

MASSACHUSETTS INSTITUTE OF TECHNOLOGY

Lexington, Massachusetts

DTIC QUALITY INSPECTED 1

This technical report has been reviewed and is approved for publication.

FOR THE COMMANDER

Gary Tutungian
Administrative Contracting Officer
Contracted Support Management

MASSACHUSETTS INSTITUTE OF TECHNOLOGY
LINCOLN LABORATORY

SOLID STATE RESEARCH

QUARTERLY TECHNICAL REPORT

1 FEBRUARY — 30 APRIL 1994

ISSUED 9 SEPTEMBER 1994

By

Di: t

Av

Dist | A

A-1

LEXINGTON

MASSACHUSETTS

ABSTRACT

This report covers in detail the research work of the Solid State Division at Lincoln Laboratory for the period 1 February through 30 April 1994. The topics covered are Electrooptical Devices, Quantum Electronics, Materials Research, Submicrometer Technology, High Speed Electronics, Microelectronics, and Analog Device Technology. Funding is provided primarily by the Air Force, with additional support provided by the Army, ARPA, Navy, BMDO, NASA, and NIST.

TABLE OF CONTENTS

LIST OF ILLUSTRATIONS

LIST OF ILLUSTRATIONS (Continued)

LIST OF ILLUSTRATIONS (Continued)

LIST OF TABLES

INTRODUCTION

1. ELECTROOPTICAL DEVICES

The first precision GaAs microlenses with large numerical apertures have been fabricated using one-step ion-beam-assisted etching followed by mass-transport smoothing. Mass transport was carried out in a specially designed reactor in which only a small amount of As is needed for the vapor protection of GaAs.

Improvements in epitaxial growth and device design for 1.3-μm strained-layer lasers with three quantum wells have yielded threshold current densities < 200 A/cm^2, differential quantum efficiencies $> 80\%$, and very high net modal gains. Preliminary ridge-waveguide laser results have also been obtained.

The first InP-based tapered lasers have been demonstrated, which achieved continuous output powers of 0.5 W with nearly 80% power in the central lobe. This represents a significant improvement in brightness of 1.3-μm sources.

2. QUANTUM ELECTRONICS

Passively Q-switched 1.06-μm microchip lasers have been constructed from thin pieces of Nd^{3+}:YAG bonded to thin pieces of Cr^{4+}:YAG. When pumped with the unfocused, 1.2-W output of a fiber-coupled diode, these devices produced 11-μJ pulses of 337-ps duration at a pulse repetition rate of 6 kHz in a single-frequency, TEM$_{00}$ mode.

Multiply passing 1.064- and 1.319-μm laser beams through a LiB$_3$O$_5$ crystal has been demonstrated to coherently enhance the sum-frequency generation of sodium-resonance radiation at 0.589 μm. An enhancement of a factor of 3.8 in the generated yellow power was obtained for three passes.

An investigation has been made of the mechanical failure of coatings involving ZnS/modified-CeF$_3$ thin films on fused silica for use within a diode-pumped Ho:YAG laser system. The failures were shown to be a result of tensile stress at the substrate/film interface induced by a large differential in thermal expansion coefficients.

3. MATERIALS RESEARCH

Double-heterostructure InAsSb/AlAsSb diode lasers emitting at $\sim$ 3.9 μm have exhibited pulsed operation at temperatures up to 170 K and CW operation up to 105 K, with single-ended CW output power of 30 mW at 70 K. The lowest pulsed threshold current density was 36 A/cm^2 obtained at 60 K.

GaSb grown by low-pressure organometallic vapor phase epitaxy using triethylgallium (TEGa) and trimethylantimony (TMSb) has been found to have improved growth characteristics and materials properties compared to GaSb grown with trimethylgallium and TMSb. The epitaxial growth rate with TEGa was temperature independent between 525 and 625°C, and unintentionally doped TEGa-grown layers were p-type with hole concentration as low as 3.4×10^{15} cm^{-3} and hole mobility as high as 5.4×10^3 cm^2/V s at 77 K.

4. SUBMICROMETER TECHNOLOGY

A scalable vertical device structure and voltage programmable link have been investigated for fabricating an ultradense programmable read-only memory. Conventional i-line lithography was used to fabricate arrays of 0.6-μm-diam transistors and links, and phase-shift lithography was employed for 0.3-μm-diam devices.

The electron emission from diamond has been enhanced by depositing Cs on the sample surface after it had been exposed to O_2 or H_2 plasma discharge, but of those two preexposures, only the O_2 discharge results in an enhancement that is not degraded by subsequent heating and exposure to O_2. A model that explains these results is proposed.

5. HIGH SPEED ELECTRONICS

Resonant tunneling diodes (RTDs) fabricated in the pseudomorphic $In_{0.53}Ga_{0.47}As/AlAs$ material system on GaAs substrates have demonstrated peak-to-valley current ratios (PVCRs) of ~ 9 and peak voltages of ~ 1 V at room temperature. This PVCR is 50% greater than for any reported RTD using the lattice-matched AlGaAs/GaAs or AlAs/GaAs material system.

6. MICROELECTRONICS

A procedure has been developed involving careful attention to furnace steps and materials in fabrication of charge-coupled devices (CCDs) on float-zone Si for use in imaging high-energy x-rays. By avoiding inclusion of dislocations in the CCD, which degrade charge-transfer efficiency and introduce areas of higher dark current, the method results in superior device performance.

7. ANALOG DEVICE TECHNOLOGY

The architecture and operating principles of a direct-sequence-encoded spread-spectrum modem based on superconductive electronics have been investigated. The high speed and low power of superconductive circuits are expected to increase the bandwidth by orders of magnitude over that achievable with semiconductor technology.

REPORTS ON SOLID STATE RESEARCH

1 FEBRUARY THROUGH 30 APRIL 1994

PUBLICATIONS

The Monolithic Optoelectronic Transistor: A New Optical Neuron Device	B. F. Aull E. R. Brown P. A. Maki K. B. Nichols S. C. Palmateer T. A. Lind	*Proc. SPIE* **2026**, 388 (1993)
Effect of Annealing on Photorefractive Damage in Titanium-Indiffused LiNbO₃ Modulators	G. E. Betts F. J. O'Donnell K. G. Ray	*IEEE Photon. Technol. Lett.* **6**, 211 (1994)
CCD Soft X-Ray Imaging Spectrometer for the ASCA Satellite	B. E. Burke R. W. Mountain P. J. Daniels M. J. Cooper V. S. Dolat	*IEEE Trans. Nucl. Sci.* **41**, 375 (1994)
High-Power GaInAsSb-AlGaAsSb Multiple-Quantum-Well Diode Lasers Emitting at 1.9 μm	H. K. Choi G. W. Turner S. J. Eglash	*IEEE Photon. Technol. Lett.* **6**, 7 (1994)
InAsSb/AlAsSb Double-Heterostructure Diode Lasers Emitting at 4 μm	S. J. Eglash H. K. Choi	*Appl. Phys. Lett.* **64**, 833 (1994)
Aperture Guiding in Quasi-Three-Level Lasers	T. Y. Fan	*Opt. Lett.* **19**, 554 (1994)
Quasi-Three-Level Lasers	T. Y. Fan	In *Solid State Lasers: New Developments and Applications*, M. Inguscio, ed. (Plenum, New York, 1994), p. 189

193-nm Resists and Lithography	R. R. Kunz R. D. Allen* M. A. Hartney M. W. Horn C. L. Keast M. Rothschild D. C. Shaver G. M. Wallraff*	*Polym. Adv. Technol.* **5**, 12 (1993)
Current Distribution in Superconducting Thin-Film Strips	L. H. Lee* T. P. Orlando* W. G. Lyons	*IEEE Trans. Appl.* *Superconduct.* **4**, 41 (1994)
Large-Numerical-Aperture Microlens Fabrication by One-Step Etching and Mass-Transport Smoothing	Z. L. Liau D. E. Mull C. L. Dennis R. C. Williamson R. G. Waarts*	*Appl. Phys. Lett.* **64**, 1484 (1994)
Issues and Applications for Wideband Real-Time Spectral Analysis Systems	W. G. Lyons A. C. Anderson D. R. Arsenault M. M. Seaver R. R. Boisvert T. C. L. G. Sollner	*Proc. SPIE* **2156**, 88 (1994)
Effects of Phase Errors on Coherent Emitter Arrays	C. D. Nabors	*Appl. Opt.* **33**, 2284 (1994)
Molecular-Beam-Epitaxy Growth of High-Performance Midinfrared Diode Lasers	G. W. Turner H. K. Choi D. R. Calawa J. V. Pantano J. W. Chludzinski	*J. Vac. Sci. Technol. B* **12**, 1266 (1994)
Single-Spatial-Mode Tapered Amplifiers and Oscillators	J. N. Walpole E. S. Kintzer S. R. Chinn C. A. Wang L. J. Missaggia	*Proc. SPIE* **1850**, 51 (1993)

*Author not at Lincoln Laboratory.

| Adjusting Trimethylgallium Injection Time to Explore Atomic Layer Epitaxy of GaAs Between 425 and 500 C by Organometallic Vapor Phase Epitaxy | C. A. Wang D. M. Tracy | *J. Electron. Mater.* **23**, 185 (1994) |

ACCEPTED FOR PUBLICATION

A Linearized Modulator for Sub-Octave-Bandpass Optical Analog Links	G. E. Betts	*IEEE Trans. Microwave Theory Tech.*
Double-Heterostructure Diode Lasers Emitting at 3 μm with a Metastable GaInAsSb Active Layer and AlGaAsSb Cladding Layers	H. K. Choi S. J. Eglash G. W. Turner	*Appl. Phys. Lett.*
A Review of Microfabricated Devices for Gene-Based Diagnostics	M. Eggers* D. J. Ehrlich	*Hematol. Pathol.*
Preshaping Photoresist for Refractive Microlens Fabrication	T. R. Jay M. B. Stern	*Opt. Eng.*
InAs$_{1-x}$Sb$_x$/In$_{1-y}$Ga$_y$/As Multiple-Quantum-Well Heterostructure Design for Improved 4–5 μm Lasers	Z. L. Liau H. K. Choi	*Appl. Phys. Lett.*
A Simple Application of the Envelope-Function Approximation for Photonic Crystals	J. P. Mattia E. R. Brown C. D. Parker	*Phys. Rev. Lett.*
Effects of Band Nonparabolicity and Central Cell Corrections on the Spectrum of Si Donors in GaAs Quantum Wells	E. R. Mueller* D. M. Larsen* J. Waldman* W. D. Goodhue	*Phys. Rev. B*
Dry Etching for Coherent Refractive Microlens Arrays	M. B. Stern T. R. Jay	*Opt. Eng.*
Binary Optics Fabrication	M. B. Stern	*Microoptics*

*Author not at Lincoln Laboratory.

Free Space Optical Interconnection Technology in Parallel Processing Systems	D. Z. Tsang T. J. Gobhek	Opt Eng

PRESENTATIONS[†]

Diamond Field-Emitters for Flat-Panel Displays	J. C. Twichell M. W. Geis T. M. Lyszczarz	High Definition Systems Information Exchange Conference, Arlington, Virginia, 30 January–2 February 1994
Emission Spectra and Fluorescence Lifetime Measurements of Yb:YAG as a Function of Temperature	T. Y. Fan D. S. Sumida*	Advanced Solid-State Lasers Meeting, Salt Lake City, Utah, 7-10 February 1994
Low-Power Adaptive Filter	A. M. Chiang	International Solid-State Circuits Conference, San Francisco, California, 16-18 February 1994
Oil-Thickness Detection Using Wideband Radiometry	O. B. McMahon E. R. Brown G. M. Daniels T. J. Murphy	International Oil Spill Conference, Long Beach, California, 27 February 1994
Materials Evaluation of Antireflective Coatings for Single-Layer 193-nm Lithography	R. R. Kunz R. D. Allen*	SPIE Symposium on Microlithography '94, San Jose, California, 28 February–5 March 1994

---

*Author not at Lincoln Laboratory.
[†]Titles of presentations are listed for information only. No copies are available for distribution.

Diamond Field Emission Cathodes	M. W. Geis J. C. Twichell C. O. Bozler N. N. Efremow K. E. Krohn T. M. Lyszczarz R. S. Uttaro M. Kordesch* J. Macaulay*	
Experimental Evidence for the Creation of Vortices at Microwave Frequencies	P. P. Nguyen* D. E. Oates G. Dresselhaus* M. S. Dresselhaus*	March Meeting of American Physical Society, Pittsburgh, Pennsylvania, 21-25 March 1994
Frequency Dependence of Z_s for $YBa_2Cu_3O_{7-x}$ Thin Films in dc Magnetic Fields: Investigation of Vortex Dynamics	S. Revenaz D. E. Oates G. Dresselhaus*	
Broadband Far-Infrared Spectroscopy of Mesoscopic Devices	S. Verghese* R. Wyss* T. H. Schapers* Q. Hu* E. R. Brown A. K. McIntosh	
Optical Interconnections and Smart Pixels	R. C. Williamson	DoD Fiber Optics and Photonics Conference, McLean, Virginia, 22-24 March 1994
A Comparison of Iron Concentration and Photorefractive Gain in Iron- Doped Indium Phosphide	D. F. Bliss* G. Bryant* G. W. Iseler B. Johnson F. X. Zach*	Indium Phosphide and Related Materials, Santa Barbara, California, 27-31 March 1994

---

*Author not at Lincoln Laboratory.

Diamond Field-Emission Cathodes	M. W. Geis J. C. Twichell C. O. Bozler N. N. Efremow K. E. Krohn T. M. Lyszczarz R. S. Uttaro M. Kordesch* J. Macaulay*	1994 Tri-Service/NASA Cathode Workshop, Cleveland, Ohio, 29-31 March 1994
An Ultra-Wideband Photonic Crystal	K. Agi* E. R. Brown C. Dill III O. B. McMahon K. J. Malloy* G. Hover*	Second International Conference on Ultra-Wideband, Short-Pulse Electromagnetics,
Ultrawideband Coherent Generation in an LTG-GaAs Photomixer	E. R. Brown K. A. McIntosh K. B. Nichols M. J. Manfra C. L. Dennis M. Melloch*	Brooklyn, New York, 5-7 April 1994
Microchip Lasers	J. J. Zayhowski	Lincoln Laboratory Technical Seminar Series, Carnegie-Mellon University, Pittsburgh, Pennsylvania, 7 April 1994
Progress in Mid-Infrared Diode Lasers at MIT Lincoln Laboratory	H. K. Choi G. W. Turner Z. L. Liau D. L. Spears	7th Annual Diode Laser Technology Conference, Fort Walton Beach, Florida, 19-21 April 1994

*Author not at Lincoln Laboratory.

Optically Pumped 3–5 μm Semiconductor Lasers

Optically Pumped 3–5 μm Semiconductor Lasers	H. Q. Le
	G. W. Turner
	W. D. Goodhue
	P. A. Maki
	C. Dill III
	J. R. Ochoa
	J. J. Zayhowski
	A. Sanchez
	Z. Feit*

7th Annual Diode Laser Technology Conference, Fort Walton Beach, Florida, 19-21 April 1994

1.9-μm Diode-Laser-Pumped, 2.1-μm Ho:YAG Laser	C. D. Nabors
	J. R. Ochoa
	T. Y. Fan
	A. Sanchez
	H. K. Choi
	G. W. Turner

Vacuum Microtriode Development	C. O. Bozler	Lincoln Laboratory Technical Seminar Series, Rensselaer Polytechnic Institute, Troy, New York, 25 April 1994
	D. D. Rathman	
	M. W. Geis	

Integrated Optics	L. M. Johnson	Lincoln Laboratory Technical Seminar Series, Dartmouth College, Hanover, New Hampshire, 29 April 1994

---

*Author not at Lincoln Laboratory.

ORGANIZATION

SOLID STATE DIVISION

A. L. McWhorter, *Head*
I. Melngailis, *Associate Head*
D. C. Shaver, *Associate Head*
J. F. Goodwin, *Assistant*

D. J. Ehrlich, *Senior Staff*
E. Stern, *Senior Staff*
C. L. Keast, *Staff*
N. L. DeMeo, Jr., *Associate Staff*
J. W. Caunt, *Assistant Staff*
K. J. Challberg, *Administrative Staff*

SUBMICROMETER TECHNOLOGY

M. Rothschild, *Leader*
T. M. Lyszczarz, *Assistant Leader*
L. H. Dubois, *Senior Staff*[†]

Astolfi, D. K.	Hartney, M. A.[†]
Craig, D. M.	Horn, M. W.
Dennis, C. L.	Kunz, R. R.
DiNatale, W. F.	Maki, P. A.
Doran, S. P.	Palmateer, S. C.
Efremow, N. N., Jr.	Sedlacek, J. H. C.
Forte, A. R.	Stern, M. B.
Geis, M. W.	Twichell, J. C.
Goodman, R. B.	Uttaro, R. S.

QUANTUM ELECTRONICS

A. Sanchez-Rubio, *Leader*
T. Y. Fan, *Assistant Leader*

Aggarwal, R. L.	Hsu, L.*
Cook, C. C.	Jeys, T. H.
Daneu, V.	Kelley, P. L.‡
DeFeo, W. E.	Le, H. Q.
DiCecca, S.	Ochoa, J. R.
Dill, C., III	Zayhowski, J. J.

ELECTRONIC MATERIALS

B-Y. Tsaur, *Leader*
D. L. Spears, *Assistant Leader*

Chen, C. K.	Krohn, L., Jr.
Choi, H. K.	McGilvary, W. L.
Connors, M. K.	Nitishin, P. M.
Fahey, R. E.	Pantano, J. V.
Finn, M. C.	Paul, S. A.*
Golovchenko, P. A.	Reinold, J. H., Jr.
Harman, T. C.	Turner, G. W.
Iseler, G. W.	Wang, C. A.

HIGH SPEED ELECTRONICS

M. A. Hollis, *Leader*
E. R. Brown, *Assistant Leader*
R. A. Murphy, *Senior Staff*

Bozler, C. O.	Mathews, R. H.
Chen, C. L.	Mattia, J. P.*
Goodhue, W. D.	McIntosh, K. A.
Harris, C. T.	McMahon, O. B.
Lincoln, G. A., Jr	Nichols, K. B.
Mahoney, L. J.	Rabe, S.
Manfra, M. J.	Rathman, D. D.

---

* Research Assistant
[†] Intergovernmental Personnel Act assignment
‡ Leave of Absence

1. ELECTROOPTICAL DEVICES

1.1 FABRICATION OF GaAs MICROLENSES BY SURFACE-ENERGY-INDUCED MASS TRANSPORT

Precision microlenses with large numerical apertures have recently been fabricated in GaP by using a simple one-step ion-beam-assisted etching followed by surface-energy-induced mass-transport smoothing [1],[2]. These microlenses are of considerable interest for efficient collimation and focusing of heterostructure laser outputs. Fabrication of such microlenses in GaAs would further facilitate the desired monolithic integration with lasers. Here, we report the design and testing of a reactor suitable for GaAs mass transport and describe the fabrication of the first GaAs microlenses.

As illustrated in Figure 1-1, the present reactor utilizes solid As to provide the As vapor pressure needed for preventing the GaAs decomposition. This avoids the severe safety hazard of using AsH_3 gas. To further minimize the As consumption, the reactor is equipped with an inner tube with tapered end regions which, after an initial baking and purging, can be pushed in to form tight seals to minimize the As outdiffusion. The remaining solid As in the inner tube sublimes and condenses in the cooler region just outside the furnace, where a Au-coated hemispherical partial reflector is installed to facilitate As temperature control and monitoring.

Prior to each run, lens preforms shown in Figure 1-2(a) were fabricated in a (001) GaAs wafer by using photolithography and ion-beam-assisted etching. The wafer was then cleaned in H_2SO_4, lightly chemically etched in H_2SO_4:H_2O_2:H_2O (5:1:1), and loaded into the prebaked reactor, in which the wafer was totally surrounded by sapphire plates. Less than 1 g of solid As was loaded in the As basket (made of quartz, as the rest of the reactor tubes), but the tapered seals were not engaged in order to allow H_2
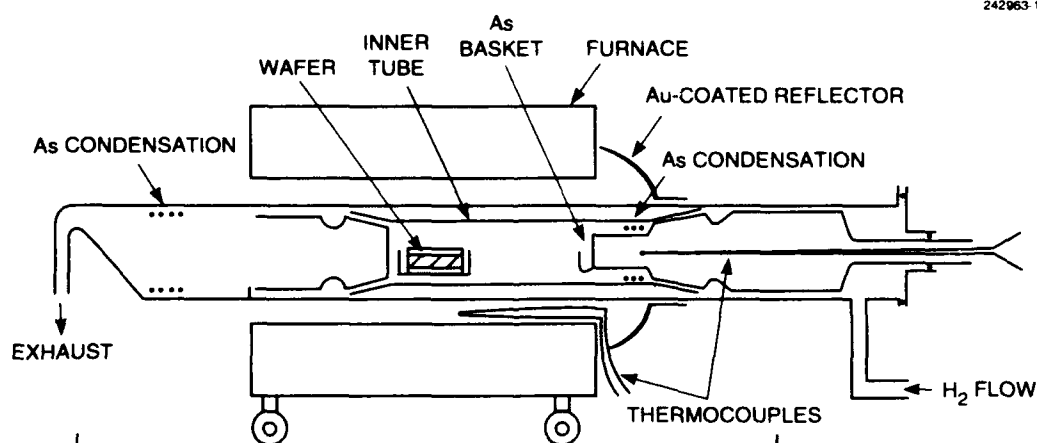
Figure 1-1. Reactor design for GaAs mass-transport process. The inner tube with tapered seals allows for sufficient As vapor pressure with minimum As consumption.

1
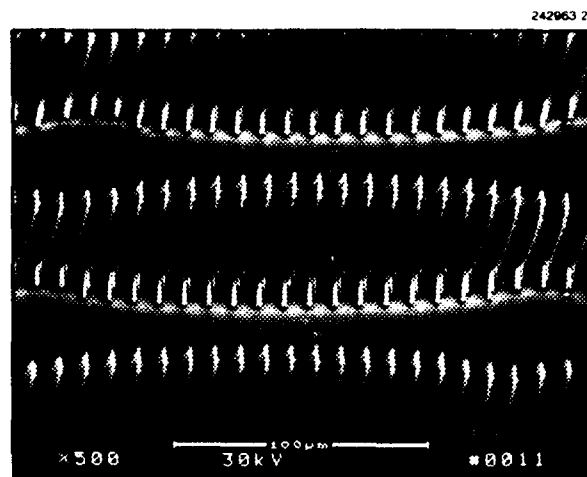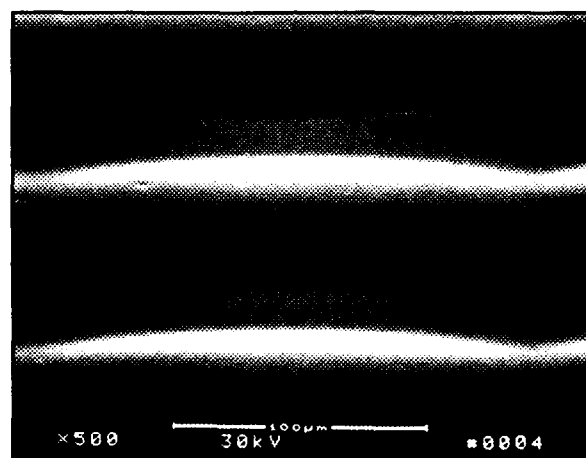
Figure 1-2. Scanning electron micrographs of GaAs microlens fabrication: (a) multiple-mesa lens preform produced by ion-beam-assisted etching, and (b) lens formed after smoothing by surface-energy-induced mass transport. These views show one lens in the center with adjacent rows of lenses partially seen. The center-to-center spacing between rows is 200 mm.

to flow through the inner tube. The furnace was heated to 950°C; the As basket being in a cooler region was 500°C. After approximately 1 h nearly 80% of the As had been evaporated and purged to the rear end of the outer tube. The tapered seals were pushed together tight to enclose the inner tube. The furnace position was then fine adjusted for a desired As temperature of ~ 350°C, at which the atmospheric pressure of the As vapor is 5×10^{-4} [3]. This was sufficient protection for the GaAs wafer, whose surface was very smooth and free from any damage after over 100 h at 950°C.

242963-3

HEIGHT (μm)

8 —

6 —

4 —

2 —

0 —

-100   -50   0   50   100

POSITION (μm)

SLOW
DIRECTION

FAST
DIRECTION
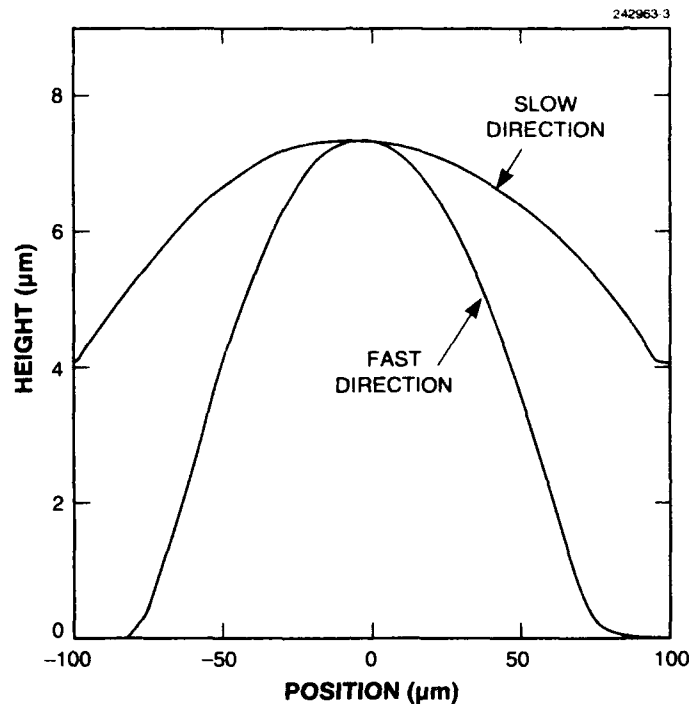
Figure 1-3. Stylus surface profiling of fabricated GaAs microlens. This lens is anamorphic, with two distinct curvatures, and is designed to collimate the astigmatic output from high-power diode lasers with a tapered gain region.

Figure 1-2(b) shows the formation of the GaAs anamorphic microlens after mass-transport smoothing. As shown in the stylus surface profiling in Figure 1-3, this lens has two distinct curvatures and is designed to collimate the astigmatic output from high-power diode lasers with a tapered gain region [4]–[6]. This design is quite similar to a previous one fabricated in GaP [2]. The achievement of a smooth lens surface and the precise lens profile control show that the GaAs mass transport is basically very similar to that of GaP and InP.

Other aspects of this arsenide work are also quite similar to the previous phosphide ones. For instance, there is strong evidence of a similar contamination problem from the quartz tubes [1], and the wafer needed to be totally surrounded by sapphire to minimize that contamination. We believe that further process optimization can result in a drastic reduction of mass-transport time. In addition, it is worth noting that the capability of fabricating microlenses in GaAs not only opens up the possibility for monolithic integration with lasers but also makes available a high-quality and more economical substrate for microoptics.

Z. L. Liau
D. E. Mull
D. L. Hovey

3

1.2 IMPROVED 1.3-μm STRAINED-LAYER InGaAsP/InP QUANTUM-WELL LASERS

Recently, results were reported on broad-area diode lasers that emitted at 1.3 μm and were made from strained-layer quantum-well (SLQW) structures of $In_{1-x}Ga_xAs_yP_{1-y}$ alloys [7]. These results were notable in that the threshold current densities and differential quantum efficiencies were comparable to the best values reported in the literature, even though the structures were grown during an early development stage of our InP-based organometallic vapor phase epitaxy (OMVPE).

Here, we report devices resulting from an effort to improve the OMVPE growth and to use a step-graded separate-confinement heterostructure (SCH). Broad-area laser characterization shows significant improvement in threshold current density, differential efficiency, and modal gain. Preliminary results for ridge-waveguide narrow-stripe lasers are also presented. In Section 1.3, the step-graded structure has been used to make the first reported InP-based tapered lasers. These give record power levels with nearly diffraction-limited beam widths.

In the present effort, two structures, both with three SLQWs but one with a flat or ungraded SCH region and the other with a step-graded SCH region, have been grown under the basic conditions described in Ref. 7. For improved uniformity across the wafer, these new structures have been fabricated on full-sized, rather than quarter-sized, 50-mm-diam substrates. For improved uniformity through the QW region, the growth rates of well and barriers regions have been lowered, something made possible by instrumentation changes for better gas metering at low flows.

In order of growth, the device structures consisted of a 1.0-μm n-type InP cladding layer grown on an n^+ InP substrate of (100) orientation, followed by growth of the lower SCH region, three 8-nm QWs having the approximate composition $In_{0.90}Ga_{0.10}As_{0.55}P_{0.45}$ under ~ 1% biaxial compression with ~ 1-nm barriers, the upper SCH region, a p-type InP cladding region 1.5 μm thick with an ~ 8-nm etch-stop layer inserted after 0.2 μm, and finally a 0.2-μm-thick p^+ contact layer of $In_{0.53}Ga_{0.47}As$. For the ungraded structure, upper and lower SCH layers consisted of 230 nm of a lattice-matched $In_{1-x}Ga_xAs_yP_{1-y}$ alloy with $y = 0.2$, corresponding to a 1.05-μm bandgap wavelength. The etch-stop and QW-barrier layers were also grown with this alloy. For the step-graded structure the outer, higher steps were 220 nm of the alloy with 1.05-μm bandgap wavelength and the lower steps were 20 nm of a lattice-matched alloy with $y = 0.3$ and 1.1-μm bandgap wavelength. Etch-stop and QW-barrier layers were grown with the latter alloy. The doping of layers in both cases was the same as reported in Ref. 7.

Fabrication and testing of broad-area lasers, whose 110-μm width was defined by etched grooves, were carried out in a fashion described in Ref. 7. The threshold current density J_{th} vs length L of lasers from the ungraded- and stepped-SCH samples is shown in Figure 1-4. The values for the devices with the stepped structure are consistently lower, apparently because of the more efficient carrier transport in the step-graded structure. At $L = 3000$ μm, J_{th} is 176 and 229 A/cm^2 for the stepped- and ungraded-SCH structures, respectively. For comparison, the earlier ungraded-SCH devices with three 10-nm wells, from Ref. 7, had $J_{th} \approx 260$ A/cm^2 at this L value. Plots of J_{th} vs $1/L$ indicate that the stepped- and ungraded-SCH devices have transparency currents J_0 of 150 and 200 A/cm^2, respectively, compared to a value of 210 A/cm^2 for the earlier devices.
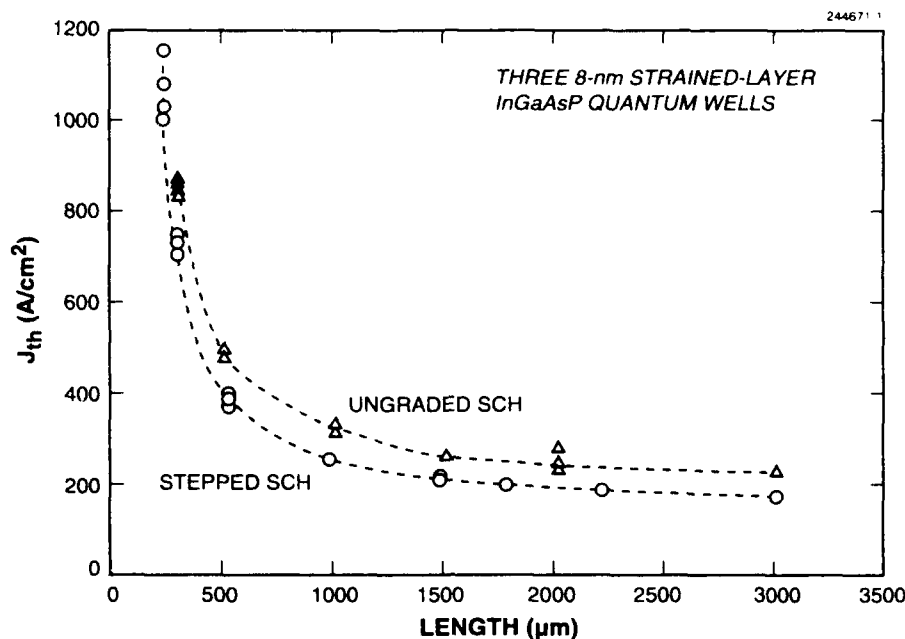
Figure 1-4. Threshold current density J_{th} vs cavity length for broad-area (110 μm wide) devices. Triangles are for devices with ungraded separate-confinement heterostructure (SCH) region and circles for devices with step-graded SCH region.

The reciprocal of the total external differential quantum efficiency, $1/\eta$, vs L is shown in Figure 1-5. For short-cavity lengths the stepped-SCH devices have somewhat lower values of η. This may be due to an increased net carrier density, and therefore higher free-carrier absorption, in the inner, smaller-bandgap SCH layers of these devices. For devices of 500-μm length, η reaches values $\geq 80\%$. To the best of our knowledge, this is significantly greater than previously reported for 1.3-μm lasers and is comparable to the highest values reported for any of the InP-based lasers. For the step-graded SCH devices, the maximum η is ~ 75% and occurs at $L = 250$ μm. Earlier devices had a maximum η of 61%, at $L = 300$ μm. If one assumes a constant total loss α that is independent of current and a constant differential radiative efficiency above threshold, η_i, one can obtain estimates of η_i and α from the intercept and slope of these results. However, these two assumptions, often made in the literature, are not justified in all cases. It is likely they fail when they lead to values of η_i significantly less than 1, which is in contradiction to the usual assumption that the gain is clamped above threshold at its threshold value [8]. Nevertheless, the values obtained from the $1/\eta$ vs L plots are useful for comparison purposes. For the step-graded structures these are $\eta_i = 0.8$ and $\alpha = 4.0$ cm^{-1}, and for the ungraded-SCH structures $\eta_i = 1.0$ and $\alpha = 6.0$ cm^{-1}. Values for the earlier material were $\eta_i = 0.7$ and $\alpha = 4.5$ cm^{-1}. A facet reflectivity of 0.29 has been used in calculating α.

Values of the net modal gain G-α vs J obtained from the J_{th} vs L results are shown in Figure 1-6; for this estimate it was assumed for each J_{th} that G-$\alpha = L^{-1}\ln R^{-1}$, where R is the facet reflectivity. Estimates of G-α, unlike G, do not require assumptions for α and η_i. As seen, very high net modal gains can be achieved.

5
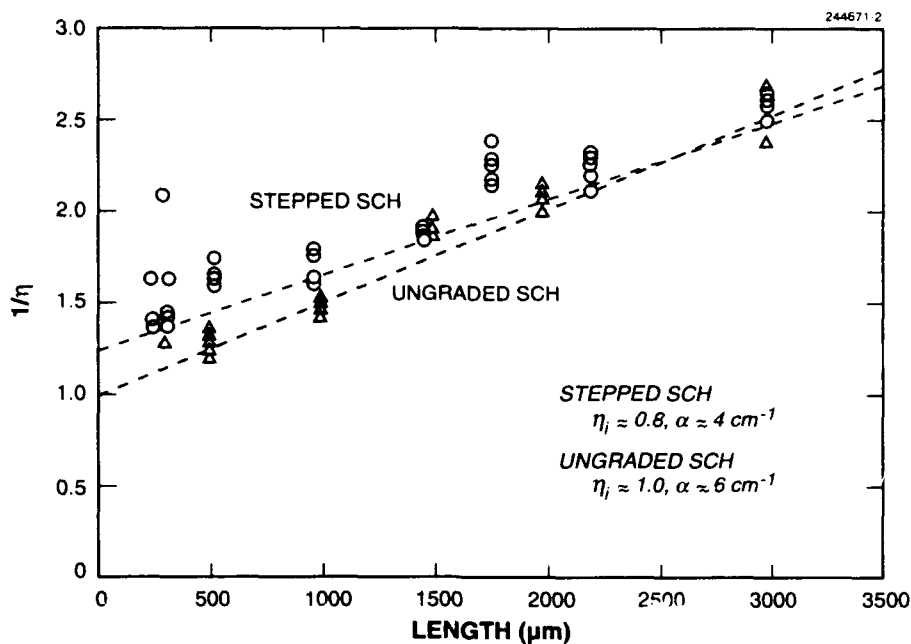
Figure 1-5. Inverse of the total differential quantum efficiency, 1/η, vs cavity length for strained-layer devices. Assigned symbols follow those of Figure 1-4.

For the stepped-SCH devices, these reach ~ 50 cm^{-1} at 1 kA/cm^2. For the ungraded-SCH devices, the net modal gain is ~ 45 cm^{-1} at 1 kA/cm^2, which is about the same as measured for the earlier devices.

Initial efforts have been made to characterize ridge-waveguide devices. To date, lasers of various lengths with 3- and 4-μm-wide stripes from the stepped-SCH material have been fabricated and characterized with uncoated facets. The ridges have been formed by first reactive ion etching (RIE) with CH$_3$ in H$_2$ and then using a selective chemical etch that removes the RIE-induced damage in the InP cladding and stops at the thin, inserted alloy layer.

Results to date on uncoated ridge-waveguide lasers are displayed in Figures 1-7 and 1-8, showing the cavity-length dependence of threshold current and inverse differential efficiency, respectively. For 500-mm-long uncoated devices, threshold currents of 14–15 mA and η values of ~ 37%/facet are observed. Threshold currents can be greatly reduced, especially for short cavity lengths, by application of high-reflectivity coatings. Most values reported are for coated devices, and this, plus variability in the number of quantum wells, makes a strict literature comparison difficult. Nevertheless, it is clear that these devices are among the best reported. Threshold currents of a few milliamperes should be possible with short devices having high-reflectivity coatings.

J. P. Donnelly   S. H. Groves
R. J. Bailey   A. Napoleone
J. D. Woodhouse

244671-3
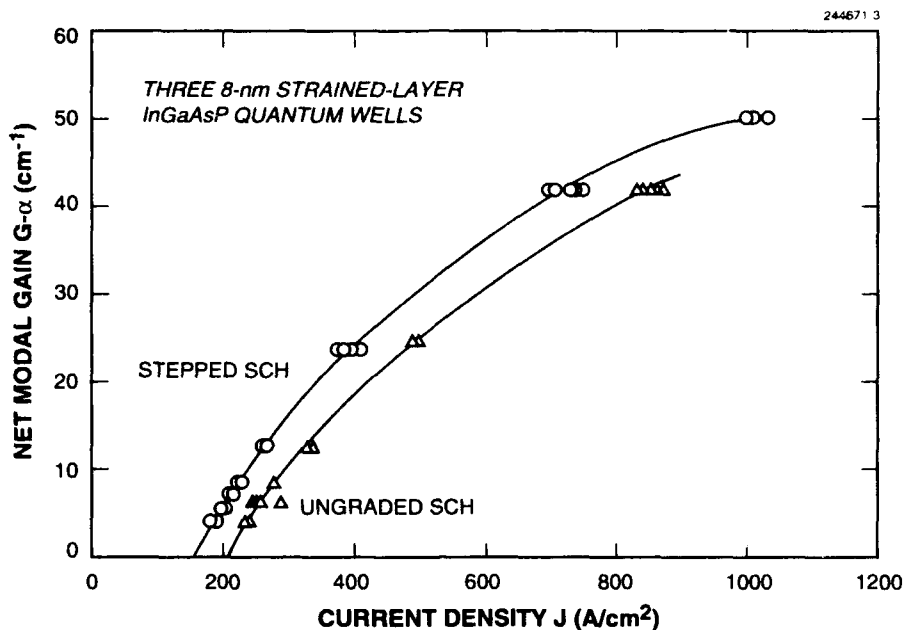
Figure 1-6. Net modal gain G-α vs current density J obtained from threshold relations for devices of varying cavity lengths. Assigned symbols follow those of Figure 1-4.

244671-4
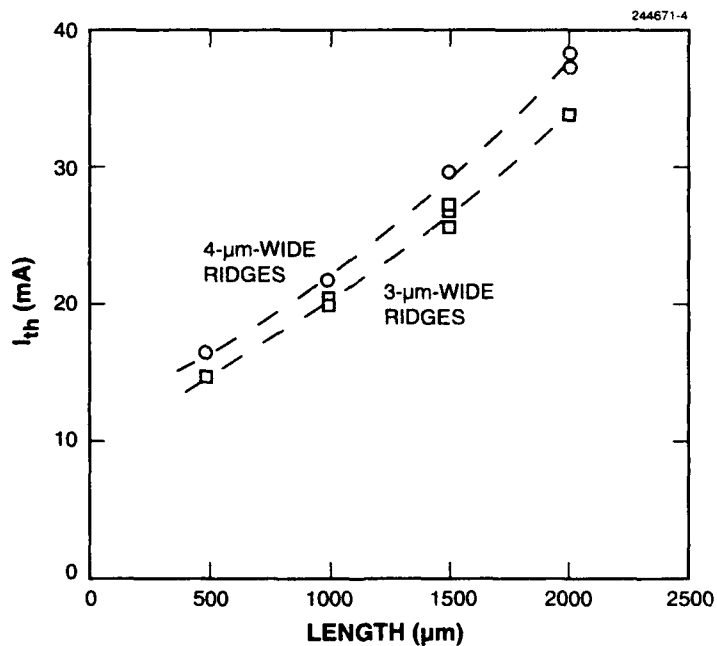
Figure 1-7. Threshold current I_{th} vs cavity length for uncoated ridge-waveguide lasers with stepped-SCH region. Squares are for devices with 3-µm-wide ridges and circles for devices with 4-µm-wide ridges.

7

40

35

η_d /FACET

30

3-µm-WIDE
RIDGES

4-µm-WIDE
RIDGES

25

20

0   500   1000   1500   2000   2500
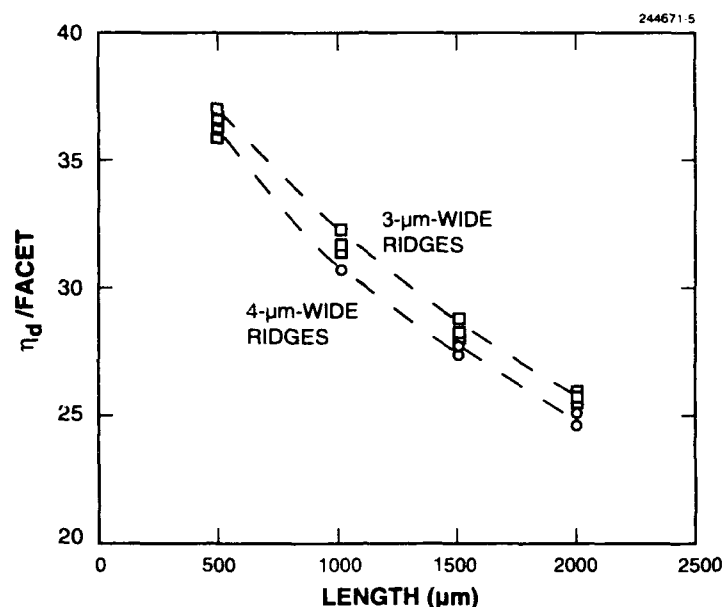
LENGTH (µm)

Figure 1-8. Differential quantum efficiency vs cavity length for uncoated ridge-waveguide lasers with stepped-SCH region. Assigned symbols follow those of Figure 1-7.

1.3 HIGH-POWER, STRAINED-LAYER DIODE LASERS WITH TAPERED GAIN REGION FOR OPERATION AT 1.3 µm

Semiconductor optical sources with a tapered gain region are well suited for applications requiring high CW power and good spatial mode quality. Such devices include high-power amplifiers, lasers, master oscillators integrated with power amplifiers, and amplifiers for optical integrated-circuit beam splitters. Successful operation of these large-area devices (typically several millimeters long by several hundred micrometers wide) requires epitaxially grown material of excellent uniformity. GaAs-based devices for use at 0.98 µm have been well demonstrated [4],[5],[9],[10], and a report has been given of 2-µm GaSb-based devices [11]. Here, we demonstrate the first InP-based tapered lasers. These devices, which operate at $\lambda \approx 1.3$ µm, have given CW output power in excess of 0.5 W with > 79% of the power in the nearly diffraction-limited central lobe. This represents a significant increase in brightness for 1.3-µm diode laser sources [12].

Materials for the tapered lasers have been grown by atmospheric pressure OMVPE using a chimney-geometry reactor that incorporates susceptor rotation to achieve good uniformity over a 50-mm-diam substrate [13]. Section 1.2 gives layer detail as well as broad-area and ridge-waveguide laser results for the wafer used here. It has three InGaAsP QWs under ~ 1% biaxial compression and a double-step SCH.

The unstable-resonator tapered-laser oscillator design was the same as that reported for the 980-nm lasers [4],[5] and is shown in Figure 1-9. The gain region is defined by the tapered contact, which is fabricated by depositing 250 nm of pyrolitic SiO_2, opening the contact pattern using standard photolithography and etching techniques, and then depositing 50 nm of Ti, 100 nm of Pt, and 200 nm of Au. The cavity-spoiling grooves depicted in the figure prevent the optical power from burning through the unpumped regions of the wafer outside the tapered region and, thereby, establishing a Fabry-Perot oscillation cavity. The grooves, which have angled sidewalls, extend through the active layer and are effective in deflecting light towards the sides of the device and towards the substrate. The grooves are formed using SiO_2 as a mask for RIE with CH_4 and H_2 gases in approximately a 1:4 ratio of flows at a pressure of 50 mTorr.

The cavity-spoiling grooves influence the beam properties of the oscillating mode, since they form an aperture from which the beam is allowed to freely diffract to fill the angular width of the tapered electrode. For an external operating wavelength of 1.3 μm the aperture chosen was ~ 8 μm for the 6° angular full width of the taper.

The ends of the cavity were cleaved at 2-mm lengths, and the facet at the large end of the taper (~ 200 μm wide) was coated with a quarter-wave layer of evaporated SiO_x. The evaporant was SiO, which was deposited in a partial vacuum into which O_2 was leaked to achieve an oxygen content in the film corresponding to a refractive index of ~ 1.83. The resulting facet reflectivity is ~ 1%. Three quantum wells were used in this design in order to achieve sufficient gain to reach threshold at low current. Large gain is required because of the relatively large cavity losses that result from both the geometric loss of the tapered design and the large output coupling loss provided by the low-reflectivity facet coating.

Figure 1-10 shows the CW output power vs current obtained from one of the lasers, indicating total output power > 0.5 W. The beam pattern measured in the plane of the junction at the maximum output power is shown in Figure 1-11. The output beam is astigmatic with the beam perpendicular to the junction appearing to diffract from a point at the output facet, while the beam in the plane of the junction appears to diffract from the aperture defined by the cavity-spoiling grooves. When Snell's law is taken into account, the beam in the plane of the junction, as seen from the output side of the device, appears to emerge from a virtual image inside the laser approximately L/n_{eff} from the output facet, where n_{eff} is the effective index of the laser medium and L is the cavity length.
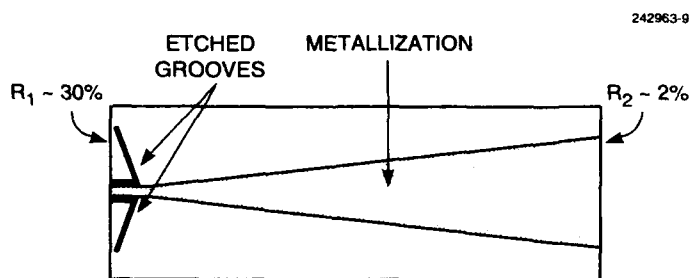
Figure 1-9. Device design of tapered laser for 1.3-μm operation. The device length is 2 mm, the spoiler aperture is ~ 8 μm, the facet at the large end is ~ 200 μm, and the full angle is 6°.
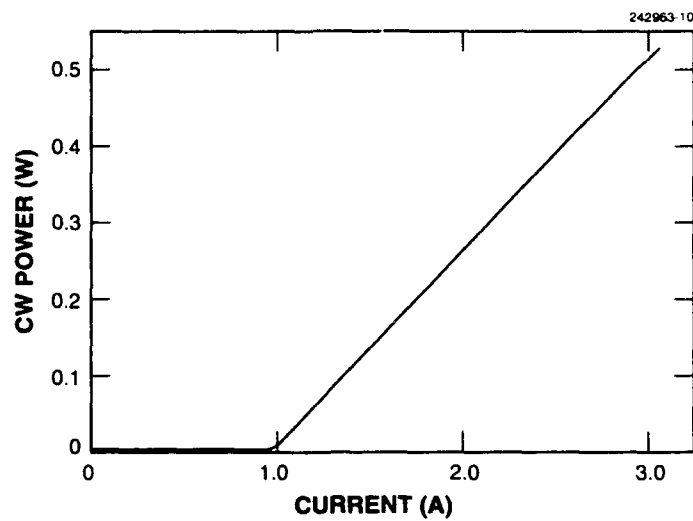
Figure 1-10. CW output power vs current for laser with tapered gain region.
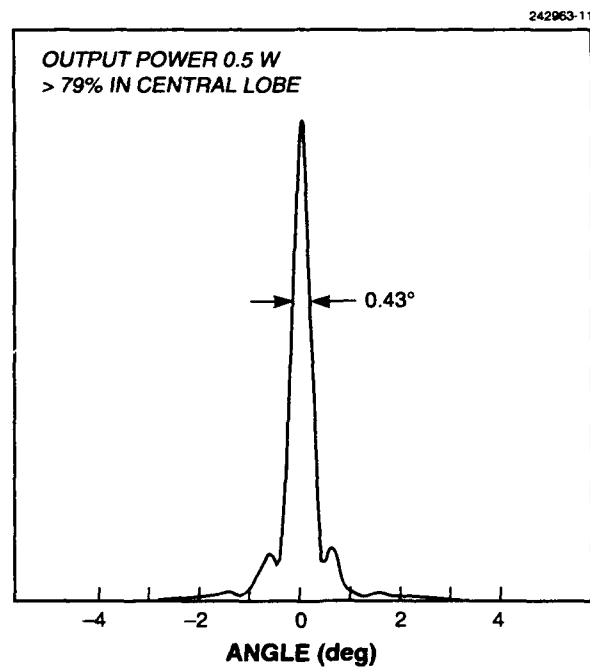
Figure 1-11. Far-field beam profile at 0.5 W for tapered laser. The power in the central diffraction lobe is > 79% of the total.

The results plotted in Figure 1-11 were obtained by first collimating the output beam in the direction perpendicular to the junction plane using a fast (f/0.83) spherical lens. This caused the beam in the other direction to be focused to a waist. The distance across the beam waist divided by the focal length of the lens gives the tangent of the angle of the beam in the far field. This far field is equivalent to the one that would result if an ideal thin cylindrical lens were placed at the output facet to exactly correct for the divergence of (i.e., collimate) the freely diffracting beam in the plane of the junction. Hence, we can directly compare the beam width as measured in Figure 1-11 with the physical dimensions of the output aperture. The expected intensity profile at the output facet is a top hat distribution, to first order, since the gain medium should be well saturated. For a 200-μm output aperture, the corresponding full width at half-maximum angular width is 0.33°. The measured value of 0.43° shown in the figure is about 1.3 times the diffraction limit. Over 79% of the 0.5 W of CW output power is contained within this central diffraction lobe. These results are similar to those obtained for the tapered 980-nm lasers and represent a significant improvement in the brightness of 1.3 μm sources.

S. H. Groves   J. P. Donnelly
J. N. Walpole   A. Napoleone
J. D. Woodhouse   L. J. Missaggia
R. J. Bailey

REFERENCES

1. Z. L. Liau, D. E. Mull, C. L. Dennis, R. C. Williamson, and R. G. Waarts, *Appl. Phys. Lett.* **64**, 1484 (1994).

2. Z. L. Liau, J. N. Walpole, D. E. Mull, C. L. Dennis, and L. J. Missaggia, *Appl. Phys. Lett.* **64**, 3368 (1994).

3. D. E. Gray (ed.), *American Institute of Physics Handbook* (McGraw-Hill, New York, 1972), p. 4–298.

4. J. N. Walpole, E. S. Kintzer, S. R. Chinn, C. A. Wang, and L. J. Missaggia, *Appl. Phys. Lett.* **61**, 740 (1992).

5. E. S. Kintzer, J. N. Walpole, S. R. Chinn, C. A. Wang, and L. J. Missaggia, *IEEE Photon. Technol. Lett.* **5**, 605 (1993).

6. D. Mehuys, D. F. Welch, and L. Goldberg, *Electron. Lett.* **28**, 1944 (1992).

7. *Solid State Research Report,* Lincoln Laboratory, MIT, 1994:1, p. 1.

8. J. N. Walpole, private communication.

9. D. F. Welch, R. Parke, D. Mehuys, A. Hardy, R. Lang, S. O'Brian, and D. Scifres, *Electron. Lett.* **28**, 2011 (1992).

10. P. S. Yeh, I. F. Wu, S. Jiang, and M. Dagenais, *Electron. Lett.* **29**, 1981 (1993).

11. H. K. Choi, J. N. Walpole, G. W. Turner, S. J. Eglash, L. J. Missaggia, and M. K. Connors, *IEEE Photon. Technol. Lett.* **5**, 1117 (1993).

12. P. J. A. Thijs, T. van Dongen, L. F. Tiemeijer, and J. J. M. Binsma, *J. Lightwave Technol.* **12**, 28 (1994).

13. S. C. Palmateer, S. H. Groves, J. W. Caunt, and D. L. Hovey, *J. Electron. Mater.* **18**, 645 (1989).

2. QUANTUM ELECTRONICS

2.1 DIODE-PUMPED PASSIVELY Q-SWITCHED PICOSECOND MICROCHIP LASERS

While coupled-cavity Q-switched microchip lasers outperform larger conventional lasers in pulsewidth, peak power, energy efficiency, and size [1], their performance is limited by the size, performance, and power consumption of the high-speed, high-voltage electronics required. In addition, performance of coupled-cavity lasers relies on maintaining interferometric control of the relative lengths of the two constituent cavities, placing tight tolerances on the manufacture of the device and on temperature control during its use.

Passively Q-switched microchip lasers do not require switching electronics, thereby reducing the size and complexity of the total system and improving the power efficiency. In addition, interferometric control of cavity dimensions is not needed, simplifying production of the device and greatly relaxing the tolerances on temperature control during its use. The result is a potentially less expensive, smaller, more robust, and more reliable Q-switched system with performance comparable to that of the coupled-cavity Q-switched microchip laser. With this combination of attributes, passively Q-switched picosecond microchip lasers are very attractive for a large range of applications including high-precision ranging, robotic vision, automated production, nonlinear frequency generation, environmental monitoring, micromachining, microsurgery, and ionization spectroscopy.

Passively Q-switched lasers typically have a pulsewidth of tens of nanoseconds, although recently pulses of 3.5-ns duration [2] have been demonstrated using a miniature laser constructed from a gain medium that simultaneously acts as a saturable absorber. With a properly optimized passively Q-switched system, it is possible to obtain pulses at least an order of magnitude shorter.

The principle behind the operation of a passively Q-switched laser is that an intracavity saturable absorber prevents the onset of lasing until the average inversion density within the cavity, N_0, reaches a value of

$$N_0 = \frac{\gamma_{sat,rt} + \gamma_{par,rt} + \gamma_{op}}{\sigma l_{rt}} \quad ,$$

$$(2.1)$$

where σ is the emission cross section at the lasing wavelength, l_{rt} is the round-trip path length of light within the cavity, $\gamma_{sat,rt} = -\ln(1 - \Gamma_{sat,rt})$ is the round-trip saturable loss constant, $\Gamma_{sat,rt}$ is the round-trip saturable loss, $\gamma_{par,rt} = -\ln(1 - \Gamma_{par,rt})$ is the round-trip unsaturable intracavity parasitic loss constant, $\Gamma_{par,rt}$ is the round-trip unsaturable intracavity parasitic loss, $\gamma_{op} = -\ln(1 - \Gamma_{op})$ is the output coupling loss constant, and Γ_{op} is the transmission through the output coupler. The onset of lasing, at this point, produces a high intracavity optical field that quickly saturates the saturable component of the loss, increasing the cavity Q and resulting in a Q-switched output pulse.

If the cross section of the saturable absorber ($\sigma_{sat} = \gamma_{sat,rt}/N_{sat}l_{rt}$, where N_{sat} is the average density of saturable absorber sites within the cavity) is much greater than the cross section of the lasing transition, the change in the cavity Q can be modeled as instantaneous [3]. In this case the resulting pulsewidth is [4]

13

$$t_w = \frac{S_p t_{rt}}{\gamma_{sat,rt}} \left[\frac{\delta(1+\delta)\eta}{\delta - \ln(1+\delta)} \right] , \qquad (2.2)$$

where S_p is the pulse shape factor (typically $S_p = 0.86$ for Q-switched laser pulses [4]), t_{rt} is the round-trip time of light within the laser cavity, η is the energy extraction efficiency of the laser pulse given by the implicit relationship $\eta(1 + \delta) = -\ln(1 - \eta)$, and $\delta = \gamma_{sat,rt}/(\gamma_{par,rt} + \gamma_{op})$ is the ratio of saturable to unsaturable cavity losses. For a given amount of saturable loss the pulsewidth asymptotically approaches its minimum value of $t_w = 4S_p t_{rt}/\gamma_{sat,rt}$ in the limit of large unsaturable losses $\left(\gamma_{par,rt} + \gamma_{op} \gg \gamma_{sat,rt} \right)$. However, this minimum pulsewidth is obtained at the expense of high threshold and low efficiency. In the opposite limit $\left(\gamma_{par,rt} + \gamma_{op} \ll \gamma_{sat,rt} \right)$ the pulsewidth asymptotically approaches $t_w = S_p t_{rt}/\left(\gamma_{par,rt} + \gamma_{op} \right)$, the threshold of the laser is reduced, and the extraction efficiency is high. The best compromise between pulsewidth, threshold, and efficiency will depend on the application of the laser.

At pump powers well in excess of threshold the period between the output pulses of a CW-pumped laser is approximately

$$t_p = \frac{\tau P_{abs,thresh}}{P_{abs}} , \qquad (2.3)$$

where τ is the spontaneous lifetime of the gain medium, P_{abs} is the total amount of pump power absorbed within the lasing mode volume, and $P_{abs,thresh}$ is the pump power required to reach the threshold inversion density given in Equation (2.1).

The picosecond Q-switched microchip laser used in the experiments reported here was constructed from a short piece of gain medium (Nd^{3+}:YAG) bonded to a solid-state saturable absorber (Cr^{4+}:YAG [5]), as shown in Figure 2-1. Both materials are polished flat and parallel on the two faces normal to the cavity axis. The pump-side face of the gain medium is coated dielectrically to transmit the pump light (808 nm) and to be highly reflecting at the oscillating frequency (1.064 μm). The facets at the interface between the two materials are coated dielectrically such that the interface is totally transmitting at the oscillating wavelength and highly reflecting at the pump wavelength. The output face of the saturable absorber is coated to be partially reflecting at the lasing frequency and provides the optical output from the device.

In one experiment the gain medium was a 0.5-mm-long piece of Nd^{3+}:YAG doped at 1.8 at.%. The saturable absorber was a 0.25-mm-long piece of Cr^{4+}:YAG doped at 0.6 at.%, with a room-temperature unsaturated absorption coefficient of 5.7 cm^{-1} and a contrast ratio $\gamma_{sat,rt}/\gamma_{par,rt}$ of ~ 6. The pump diode was coupled to the Q-switched laser through a 100-μm-core fiber with a numerical aperture of 0.37. No focusing optics were used between the fiber and the laser. The output coupler had a reflectivity of 94% and the laser reached threshold at an incident pump power of 0.8 W. When pumped with 1.2 W of incident power, the output of the laser consisted of 11-μJ pulses of 337-ps duration (full width at half-maximum), as shown in Figure 2-2. The difference between the measured pulsewidth and the expected pulsewidth of 200 ps [Equation (2.2)] is attributed to thermal effects within the active cavity. The laser oscillated in a single-frequency, TEM$_{00}$ mode at a pulse repetition rate of 6 kHz. The peak power of the

14

pulse, as derived from the pulse energy, pulse duration, and theoretical pulse shape [4], was 28 kW. With a lasing mode radius of ~ 70 μm [6] the unfocused peak output intensity is > 180 MW/cm^2. The pulse-to-pulse amplitude jitter and interpulse timing jitter were < 0.5%.
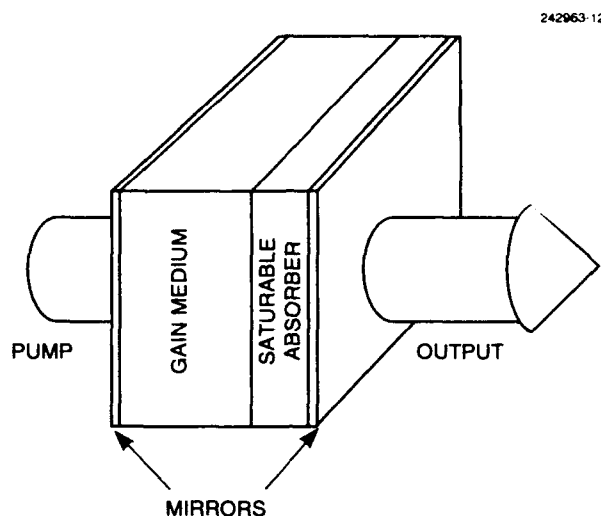
Figure 2-1. Illustration of a passively Q-switched microchip laser.
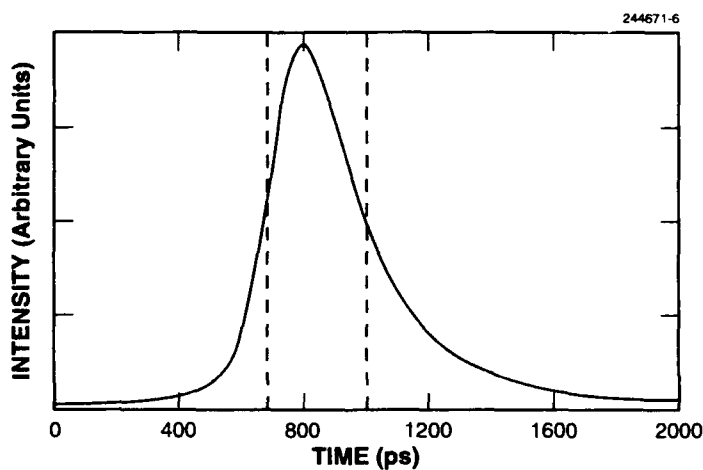
Figure 2-2. Oscilloscope trace of a 337-ps pulse from a passively Q-switched 1.064-μm microchip laser. Vertical dotted lines mark the half-maxima.

15

The peak output intensities of the passively Q-switched picosecond microchip lasers are sufficient to result in efficient nonlinear frequency generation in appropriate nonlinear crystals without focusing of the output beam. When a properly oriented, 5-mm-long crystal of KTP was placed ~ 1 mm from the output face of a device similar to the one just described, the second-harmonic conversion efficiency was > 70%. Under these conditions, some of the 532-nm radiation at the peak of the pulse was converted back into the infrared, resulting in the double-peaked structure at 532 nm shown in Figure 2-3(b). Less efficient harmonic conversion resulted in green pulses of 188-ps duration, as shown in Figure 2-3(c).

In order to test the performance of passively Q-switched microchip lasers at high repetition rates, a 1-mm-long device was constructed with a much smaller saturable loss ($\gamma_{sat,n} \approx 0.04$) and an output coupler with 97.5% reflectivity, resulting in a pulsewidth of 2.4 ns and a 100-mW threshold. With increased pump power the pulse repetition rate increased and the pulsewidth remained approximately constant. At pulse repetition rates > 10 kHz, however, there was a strong tendency for the pulse train to bifurcate, producing alternating strong and weak pulses. The ratio of the intensities varied depending on the exact pump power but was typically 0.9. The relative intensity jitter between every other pulse was < 1%. The timing interval between the pulses varied in accordance with the amplitudes; the period preceding a weak pulse was typically 0.9 times as long as the period preceding a strong pulse. The average interpulse period was consistent with Equation (2.3).

At higher pulse repetition rates (higher pump powers) the pulse train had a tendency to further subdivide into a train containing pulses of three or more amplitudes that replicated themselves periodically. At the highest repetition rates (70 kHz) there sometimes appeared to be an envelope of pulse amplitudes (typically 20% variation) with no apparent periodicity. This trend toward an increasing number of pulse amplitudes with increasing repetition rate was not always observed and depended strongly on the exact pump conditions. Stable pulses of uniform amplitude were observed at repetition rates up to 40 kHz, and bifurcated pulse trains were observed at repetition rates as high as 70 kHz.

J. J. Zayhowski   C. C. Cook
C. Dill III   J. L. Daneu
J. R. Ochoa

244671-7
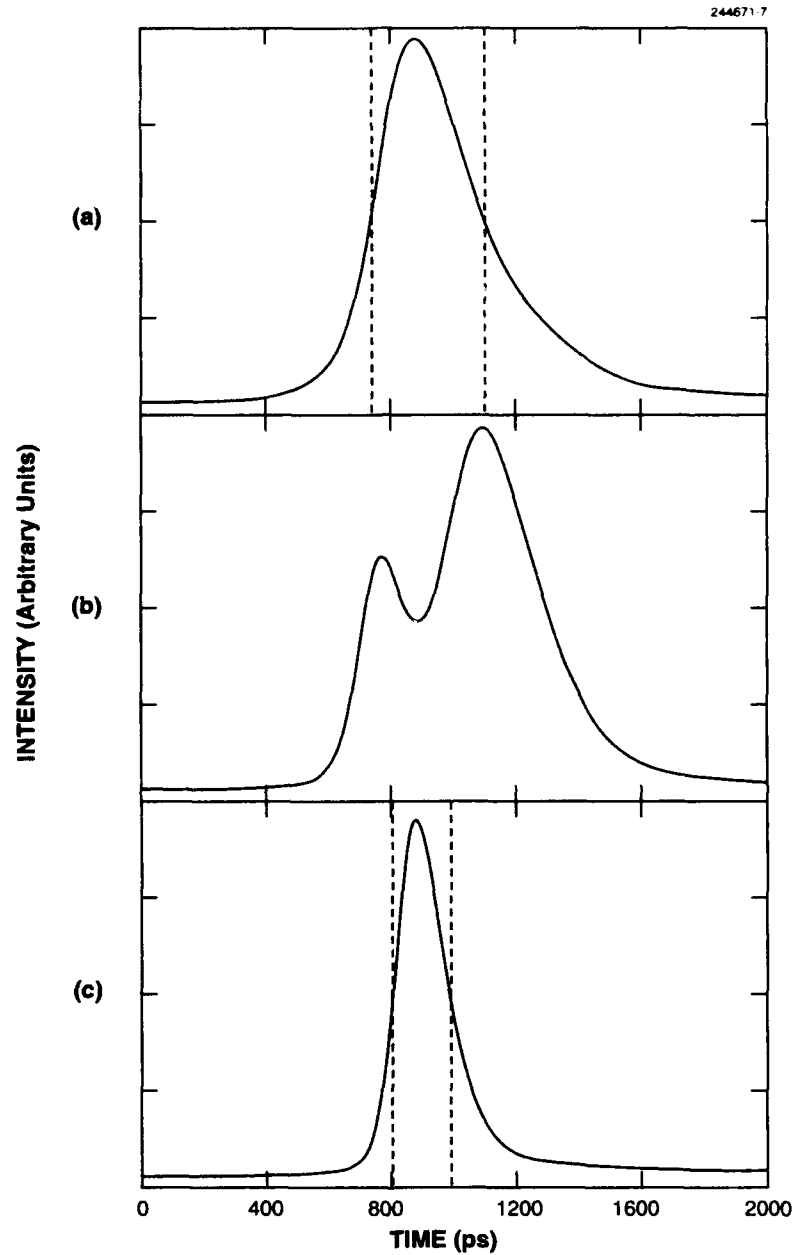
Figure 2-3. *Oscilloscope traces of (a) 363-ps, 1.064-μm pulse from a passively Q-switched microchip laser,* *(b) 532-nm pulse from infrared pulse in (a) when a 5-mm-long KTP crystal was positioned 1 mm from output face* *of laser, and (c) 188-ps, 532-nm pulse obtained through inefficient second-harmonic conversion of the pulse shown* *in (a).*

17

2.2 MULTIPLE-PASS SUM-FREQUENCY GENERATION

In the course of work aimed at generating sodium resonance radiation by mixing 1.064- and 1.319-μm laser beams, some experiments have been performed on refocusing the infrared and visible light into the nonlinear crystal for a second or third pass. For single-pass operation in a given material the limit in mixing efficiency is set by the available crystal length which establishes an optimum amount of focusing and, provided one is below damage threshold, by the available fur .iental peak power. If the latter is limited, intracavity operation is the standard avenue to further increase sum-frequency or harmonic yield. A viable multiple-pass scheme would be an attractive alternative to intracavity operation, especially for sum-frequency as opposed to harmonic generation. If crystal damage is an issue, the possibility of reaching high extraction efficiency with a relatively low power density is also attractive. Some rather stringent conditions have to be met, however, for multiple passing to be effective. First, the three beams must reenter the crystal with the appropriate wavefront, relative position, and direction to satisfy the phase-matching condition. This is already difficult when angle phase matching is used, because of the narrow acceptance angle and, more fundamentally, because of the beam walkoff inherent in the extraordinary nature of at least one of the beams. Second, the correct relative phase between the already generated sum radiation and the infrared beams has to be achieved at the second entrance into the crystal. Otherwise, reconversion to the original infrared frequencies will occur, and the second pass will cause a reduction in sum-frequency output instead of the desired gain. Because of these difficulties, previous experiments with multiple passes or multiple crystals have had mixed results [7].

When temperature, or noncritical, phase matching is used, all three interacting beams propagate like ordinary waves with no first-order walkoff effects, and further, the angular acceptance is usually quite large (several degrees). The first set of difficulties mentioned above is thus greatly reduced. Since LiB_3O_5 (LBO) can be noncritically phase matched for 589-nm generation (at 45°C), it was a good candidate for testing multiple-pass mixing.

Figure 2-4 shows two possible geometries for refocusing the light leaving the crystal for a second pass. Given the small cross section of the available crystals (3 × 3 mm), the geometry in Figure 2-4(a) presents the problem of a small angular separation between input and output beams, leading also to undesirable feedback into the lasers. However, it can be used conveniently for *two* crystals if their phase-match temperatures are close, so that both crystals can be mounted side-by-side in one oven. The geometry in Figure 2-4(b) allows the beams to return exactly through the center of the crystal with an adjustable angle to the first-pass beams. Thus, beam separation can be quite comfortable (within the angular acceptance limit), and feedback into the lasers is not a problem. This geometry also allows for a third pass by repeating the process with a second mirror-prism combination on the input side, and more passes could be accommodated if desired. Note that the schemes described here *refocus* the interacting beams after each pass. The gain expected for multiple passing is therefore higher than that due to a simple series arrangement of two or more crystals or to doubling the length of one crystal.

Small-angle glass wedges have been used to compensate delay dispersion, as shown schematically in Figure 2-4 for both geometries. For BK-7 glass a rough calculation from the dispersion results shows that the relative delay between the visible sum radiation and the infrared can be changed through one cycle (589-nm optical path) by changing the thickness of glass traversed by the interacting beams by < 100 μm; for a 2° wedge angle the required wedge translation is of the order of millimeters.

18

CRYSTAL

(a)

CRYSTAL

TOP VIEW

CRYSTAL

SIDE VIEW

(b)
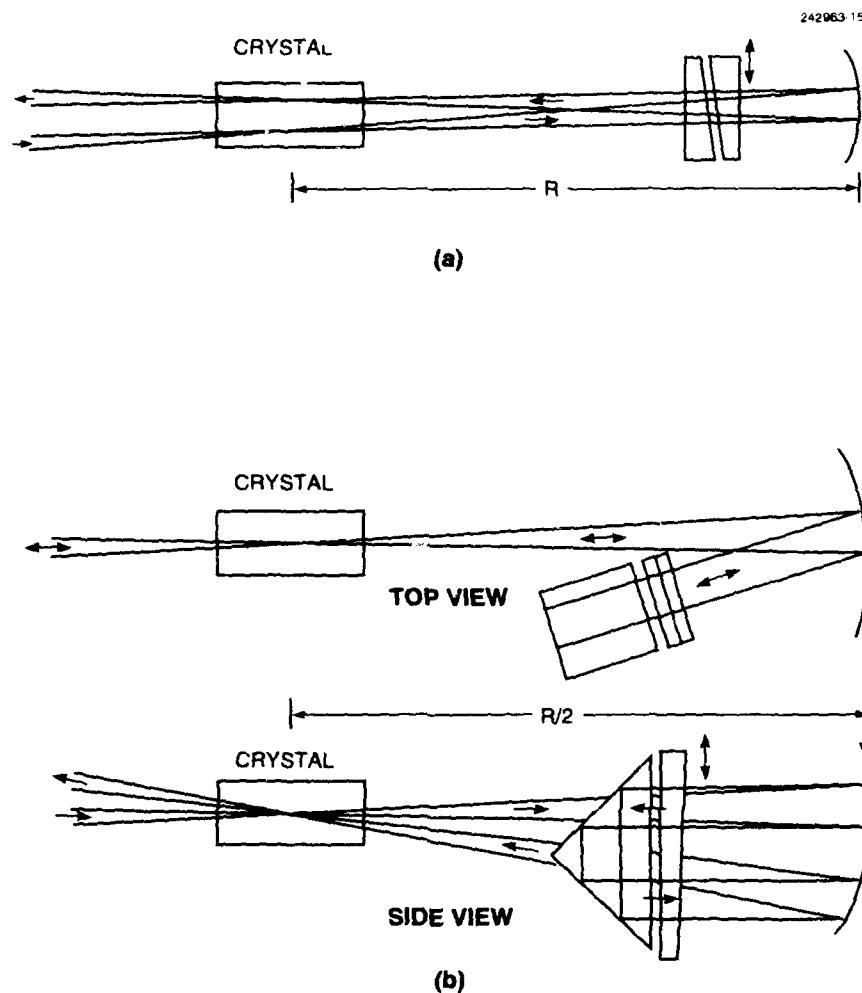
Figure 2-4. Two possible schemes for refocusing fundamental and sum-frequency beams into a nonlinear crystal: (a) center of crystal coincides with center of curvature of mirror, and (b) center of crystal is in mirror's focal plane, with the reflected beams collimated between the mirror and the 90° prism.

The issue of losses is quite crucial for the experiments described here. Both geometries in Figure 2-4 include a large number of transmission interfaces plus a mirror, the latter used twice in the geometry of Figure 2-4(b). Efficient coatings, both antireflective and highly reflective, are required at all three wavelengths. Fabrication of three-color antireflective coatings has proven to be a nontrivial problem, but a successful design has been developed that keeps the sum of the three reflectances under 1% [8]. In this respect it should be noted that for the geometry of Figure 2-4(b) the delay adjustment can be effected by varying the mirror-prism separation without the use of wedges, since the beams are collimated in the region between the mirror and the roof prism. A calculation similar to the one mentioned above, based on dispersion data for air, shows that a change in separation of the order of a few centimeters is required

19

for one cycle. The elimination of four interfaces offers a substantial advantage, but in the initial experiment the convenience of quickly adjusting the delay dispersion with a small component motion has dictated the use of wedges as shown. The LBO crystal itself was not antireflective coated, which made it the biggest source of residual loss.

The lasers utilized supplied 15 and 7 W at 1.064 and 1.319 μm, respectively, and were TEM_{00} in a quasi-CW mode with a repetition frequency of 400 Hz and 6% duty cycle. Each laser could be mode locked at 100 MHz (with a reduction in dc power of ~ 1 W), the width of the micropulses being ~ 0.5 ns at half-peak.

Both geometries shown in Figure 2-4 have been used. Double- and triple-pass experiments have been performed using one crystal, 18 mm long, with the optics of the Figure 2-4(b) geometry duplicated on the input side, in which case the input beams passed through a hole in the second folding mirror. In another experiment two crystals were used, mounted in the same oven. In this case the beams exiting the first crystal were refocused with the geometry of Figure 2-4(a) onto the second, then folded back using the geometry of Figure 2-4(b) for the third pass into the second crystal. The two experiments gave similar results as described later; the two-crystal arrangement would allow a fourth pass (through the first crystal) without any additional optics.

Results for the quasi-CW regime are shown in Figure 2-5. Power at 589 nm for the second and third passes is plotted as a function of dispersion delay. The delay is expressed as variation in glass path (referred to an arbitrary origin) as one wedge is translated along its maximum-slope line at constant speed; the power was read by a calorimeter and recorded while the wedge was moving. The first-pass 589-nm power, obviously unaffected by the delay change, was also recorded for the same interval (~ 1 min). The curve for the second-pass power clearly shows the interference of the newly generated sum radiation with that from the first pass. In the low extraction regime, and with no losses, the minima should be zero and the maxima four times the first-pass power. The actual ratio of 2.5 between second- and first-pass power at the peak of the curve is in reasonable agreement with the known residual losses. The curve for the third pass was taken with the second-pass delay held constant at its optimum value. Because of the additional losses, the reduction from the ideal value at the top of the curve is more marked, with the ratio to the first-pass power being 3.8 instead of 9. However, a substantial gain (×1.5) is still obtained over the second pass.

Figure 2-6 shows similar results for mode-locked operation of the lasers. As sum-frequency extraction from the fundamental beams becomes appreciable, the double- and triple-pass gains are reduced, but the overall advantage of multiple passing is still considerable, being 4.5 W for the third-pass 589-nm power compared with 2.1 W for one pass.

The experiments described show that multiple passing can indeed yield a substantial advantage in sum-frequency, or harmonic, generation. For practical applications, additional work in reducing losses would make the technique even more attractive. Besides the obvious step of antireflection coating the mixing crystal, the use of air dispersion instead of glass wedges has already been mentioned. With lower losses, it is likely that a higher number of passes could be used effectively.

V. Daneu

20
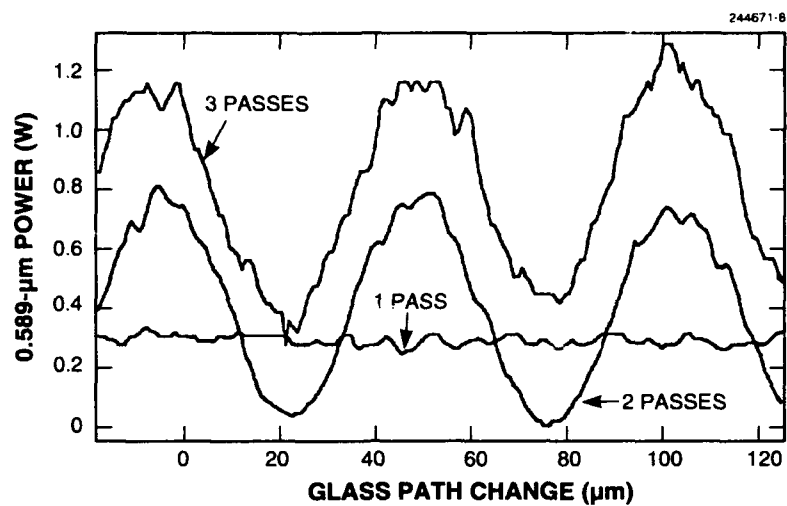
Figure 2-5. *Plots of 589-nm power exiting* LiB_3O_5 *(LBO) crystal after one, two, and three passes for non-mode-locked operation.*
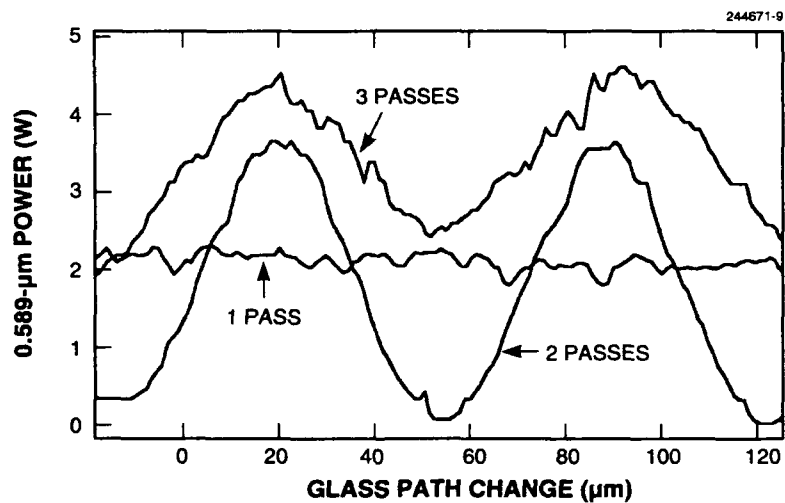
Figure 2-6. *Plots of 589-nm power exiting LBO crystal after one, two, and three passes for mode-locked operation.*

21

2.3 SUBSTRATE CONSIDERATIONS FOR 2.0-μm OPTICAL COATINGS

Beam splitters, dichroics, and output couplers for use in the 2.0-μm wavelength range are frequently coated on fused silica because of its mechanical stability, availability, and relatively low cost. In our recent experience, coatings such as Brewster-angle polarizing beam combiners that require many more layers to fabricate invariably underwent mechanical failure after removal from the coating chamber. These failures included cracking, crazing, and localized delamination. Several unsuccessful attempts were made to eliminate the failures by improving the surface preparation of the substrates using more elaborate cleaning techniques and even ion milling prior to evaporation. When no improvements were realized, a simple experiment was devised to help determine the apparent underlying film/substrate incompatibility and perhaps lead to a possible solution.

The experiment involved many different substrate materials that received the same coating under the same conditions. As a selection rule we considered only those substrates that were deemed lossless for 1.9–2.1-μm radiation, manufacturable into 2-in.-diam flats, and readily available. The test substrates chosen were fused silica (1- and 2-in.-diam flats), BaF_2, CaF_2, Dynasil, Infrasil, sapphire, and ZnSe (Dynasil and Infrasil are trade names for alternatively processed fused silica substrates). A soda-lime (float-glass) substrate served as a control piece for the experiment. The coating chosen for the experiment was a 35-layer Brewster-angle polarizing beam combiner design using ZnS and substance IRX (a modified form of CeF_3) as coating materials. This design was known to result in coating failure when deposited onto fused silica substrates.

All but one of the substrates were prepared by deep cleaning with a suspension solution of precipitated calcium carbonate, rinsed with acetone, and blown dry with nitrogen gas. Each substrate was clipped to a stainless-steel plate and rotated at an average distance of 27 in. from an electron-beam evaporation source using a state-of-the-art thermal deposition system. A substrate temperature of 150°C was maintained during the entire deposition process.

The results of the experiment are summarized in Table 2-1, which includes the type and amount of coating defect observed. Since both 1- and 2-in.-diam fused silica substrates were known to give coating failures when cleaned normally, a more rigorous cleaning procedure was used on the 2-in.-diam substrate involving a suspension of cerium oxide instead of calcium carbonate. The results of the test verified that a deeper initial cleaning of the substrates had no significant impact on the outcome. In any case, cerium oxide should be avoided on substrates that must maintain a very precise surface figure.

As Table 2-1 shows, the substrates that resulted in failed coatings all possessed much lower coefficients of thermal expansion than those that passed the test. The coefficients of the test substrates covered such a wide range we decided that a comparison with respect to the coating materials would help establish some reasoning behind the results. The coefficient of thermal expansion of bulk ZnS is reported to be 7.9×10^{-6} K^{-1} [9]. Although the precise results on IRX are not yet available, the vast majority of its composition is CeF_3 that has a bulk expansion coefficient of 14.1×10^{-6} K^{-1} at 300 K [10].

Microscopic examination of the failed coatings showed delamination $\sim$ 100-200 μm in width along randomly oriented craze lines. The failure was most prominent on the Dynasil substrate, shown in Figure 2-7. The large cracks indicate a possible failure under tensile stress with a localized delamination of the coating around each crack or craze line.

22

TABLE 2-1

**Results of Brewster-Angle Polarizing Beam Combiner
on Various Test Substrates**

Substrate	Cleaning[a]	Results[b]	Thermal Expansion Coefficient[c] ($\times 10^{-6}$ K^{-1})	
Infrasil	$CaCO_3$	Fail, subtle crazing	0.60[d]	(150)
Fused silica 1-in. diameter	$CaCO_3$	Fail, evident crazing	0.63[e]	(150)
Fused silica 2-in. diameter	CeO	Fail, evident crazing	0.63[e]	(150)
Dynasil	$CaCO_3$	Fail, pronounced cracking	0.70[e]	(150)
BaF_2	$CaCO_3$	Pass	23[e]	(150)
CaF_2	$CaCO_3$	Pass	24[e]	(40)
Sapphire	$CaCO_3$	Pass	7.5[e]	(200)
ZnSe	$CaCO_3$	Pass	8.0[e]	(150)
Soda-lime	$CaCO_3$	Pass, control piece	9.2[f]	(0–300)

[a]Following cleaning, all substrates were rinsed with acetone and blown dry with nitrogen gas.

[b]Results show type and qualitative degree of failure. In all failed coatings localized delamination accompanied the defects.

[c]Measurement temperature in parentheses (in degrees Celsius).

[d]R. Johnson, private communication.

[e]Y. S. Touloukian, R. K. Kirby, R. E. Taylor, and T. Y. R. Lee, *Thermal Expansion: Nonmetallic Solids*, Vol. 13 of *Thermophysical Properties of Matter* (IFI/Plenum, New York, 1977).

[f]R. E. Bolz and G. L. Tuve, *CRC Handbook of Tables for Applied Engineering Science*, 2nd ed. (CRC, Boca Raton, Fla., 1987), p. 162.

The photographic results along with knowledge of the thermal expansion coefficients of both the substrates and the film suggested a strong likelihood that our coating problem was due to buildup of tensile stress in the film upon cooling. If the induced stress exceeds the binding force between the film and substrate, localized delaminations of the film may be produced in weakly bound areas until cracks occur to relieve the stress. The binding force holding the film to the substrate is usually not affected by

242963-18

160 μm
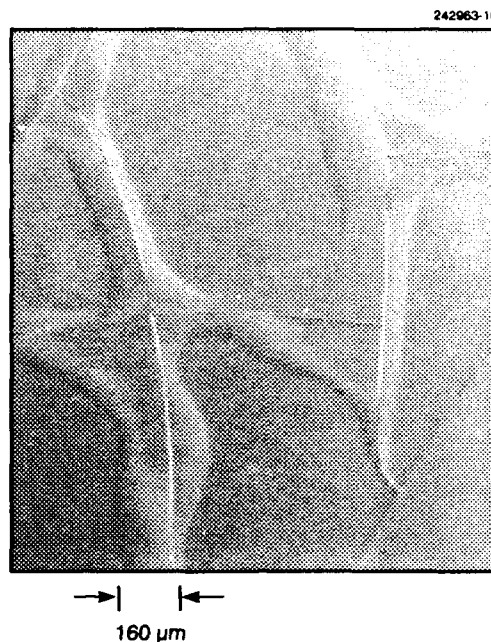
Figure 2-7. Microscopic inspection of Dynasil substrate after coating with 35-layer beam combiner using the ZnS/ IRX material system. Pronounced cracking is seen running along random directions and is usually accompanied by localized areas of delamination. A Nomarski-type microscope was used to obtain the photograph.

choice of substrate since the films are amorphous and formation temperatures are relatively low. The binding force can be affected by surface preparation, but since this was ruled out, the question as to why other coatings consisting of fewer layers did not fail still remains. The reason may be that the stack becomes more rigid as the number of layers increases, or that the multilayer itself accumulates sufficient tensile stress to cause mechanical failure with the added cooling-induced stress, or both. The buildup of intrinsic stresses in such thin-film systems is well known and usually is tensile. The relationship between lateral rigidity and the number of layers, however, is likely to depend on a great many variables and is probably difficult to predict.

In our experiment we found tensile-stress coating failures on all substrates with expansion coefficients that were very low compared to the thin-film materials. No such failures were observed on substrates having thermal expansion coefficients that were small but still within about a factor of 3 of the films. Compressive stress failure limits due to very high substrate expansion coefficients were not studied. Yet, it may be reasonable to assume a relatively higher allowable differential between the substrate and film, since the microstructure of thermally evaporated thin films is columnar [11] and under compression the voids between columns may provide a stress-relieving mechanism.

For coatings requiring a large number of layers, our results suggest that one should try to keep the thermal expansion differential between film and substrate to within about a factor of 3. Sapphire appears to be a good choice as a substrate for the fabrication of such structures.

C. C. Cook

24

REFERENCES

1. J. J. Zayhowski and C. Dill III, *Opt. Lett.* **17**, 1201 (1992).

2. S. Zhou, K. K. Lee, Y. C. Chen, and S. Li, *Opt. Lett.* **18**, 511 (1993).

3. A. Szabo and R. A. Stein, *J. Appl. Phys.* **36**, 1562 (1965).

4. J. J. Zayhowski and P. L. Kelley, *IEEE J. Quantum Electron.* **27**, 2220 (1991); **29**, 1239 (1993).

5. D. M. Andrauskas and C. Kennedy, *OSA Proc. Advanced Solid-State Lasers* **10**, 393 (1991).

6. J. J. Zayhowski, *OSA Proc. Advanced Solid-State Lasers* **6**, 9 (1991).

7. Solid State Research Report, Lincoln Laboratory, MIT, 1990:2, p. 28.

8. C. C. Cook, private communication.

9. P. W. Kruse, L. D. McGlauchlin, and R. B. McQuistan, *Elements of Infrared Technology* (Wiley, New York, 1962).

10. W. Korczak and P. Mikolaiczk, *J. Cryst. Growth* **61**, 601 (1983).

11. J. A. Thornton, *Ann. Rev. Mater. Sci.* **7**, 239 (1977).

3. MATERIALS RESEARCH

3.1 InAsSb/AlAsSb DOUBLE-HETEROSTRUCTURE 3.9-μm DIODE LASERS WITH HIGH OUTPUT POWER AND IMPROVED TEMPERATURE CHARACTERISTICS

Semiconductor diode lasers emitting in the mid-infrared (2–5 μm) band are being developed to provide efficient sources for applications such as laser radar, remote sensing, pollution monitoring, and molecular spectroscopy. Diode lasers with GaInAsSb active layers and AlGaAsSb confining layers grown on GaSb substrates are promising for high-performance sources in the 2–5-μm spectrum. For lasers emitting at ~ 2 μm, we have achieved significant improvements in room-temperature performance by employing a GaInAsSb/AlGaAsSb strained quantum-well active region and AlGaAsSb cladding layers [1],[2]. Broad-stripe lasers have exhibited pulsed threshold current density J_{th} as low as 143 A/cm^2 and single-ended CW output power as high as 1.3 W. We also reported GaInAsSb/AlGaAsSb double-heterostructure (DH) lasers emitting at ~ 3 μm that operated pulsed at temperatures up to 255 K and CW up to 170 K, with CW power of 45 mW/facet at 100 K [3].

For lasers emitting at 4 μm, we reported DH lasers with a ternary InAsSb active layer and AlAsSb cladding layers that operated pulsed up to 155 K and CW up to 80 K [4]. Even though these lasers exhibited better performance than any other III-V diode lasers with emission wavelengths > 3.5 μm, the performance was limited by substantial lattice mismatch in the laser structure. The output power at 80 K, although not accurately measured, was < 1 mW. Here, we report improved InAsSb/AlAsSb DH lasers emitting at ~ 3.9 μm. These devices have operated pulsed up to 170 K and CW up to 105 K. The maximum CW power is 30 mW, which is the highest value obtained for any diode lasers with emission wavelengths > 3 μm.

The epilayers were grown on (100)-oriented n-GaSb substrates by molecular beam epitaxy. The laser structure consists of the following layers: 0.5-μm-thick n-GaSb buffer, 3-μm-thick n-AlAs$_{0.08}$Sb$_{0.92}$ cladding, 0.8-μm-thick nominally undoped InAsSb active, 3-μm-thick p-AlAs$_{0.08}$Sb$_{0.92}$ cladding, and 0.075-μm-thick p^+-GaSb cap. Double-crystal x-ray diffraction measurement of the laser structure showed that the lattice match was better than 2.5×10^{-3}. No cross-hatch patterns were visible during inspection of the surface using Nomarski optical microscopy. The photoluminescence measured at 4.5 K had a strong peak at 3.78 μm (0.328 eV), with a full width at half-maximum of only 8 meV.

Broad-stripe lasers 60 or 100 μm wide were fabricated using SiO$_2$ patterning. Ohmic contacts to the p^+ and n GaSb were obtained by depositing Ti/Pt/Au and Au/Sn/Ti/Pt/Au, respectively, and alloying at 300°C. Individual devices 500 μm long were mounted p-side up on Cu heatsinks for pulsed measurements and p-side down on diamond submounts on Cu for CW measurements. They were then installed in a dewar for low-temperature operation.

Figure 3-1 shows the pulsed J_{th} of a 100-μm-wide device for temperatures between 60 and 170 K. At 60 K the value of J_{th} is 36 A/cm^2. The characteristic temperature T_0 for the entire temperature range is 20 K, which is higher than the 17 K observed for the previous InAsSb/AlAsSb DH lasers. The fact that a single value of T_0 describes the temperature dependence of J_{th} indicates that one dominant mechanism, most likely Auger recombination, is responsible. At the maximum operating temperature of 170 K, the value of J_{th} is 8.5 kA/cm^2, which is substantially lower than 24.4 kA/cm^2 obtained for the previous InAsSb/AlAsSb DH lasers at 155 K. We believe that these improvements are mostly due to careful lattice matching and better growth conditions.

27
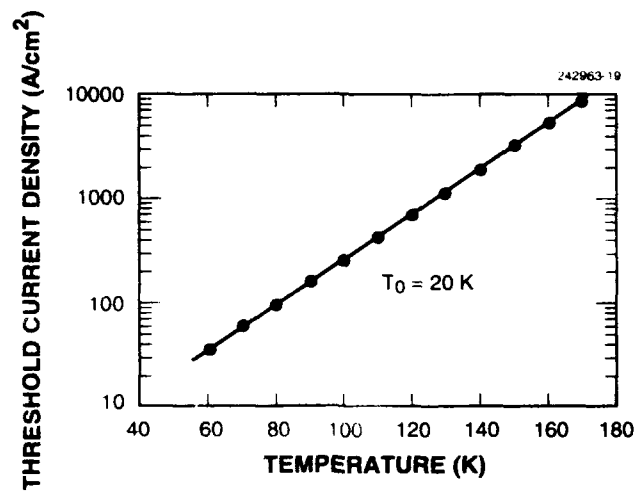
Figure 3-1. Pulsed threshold current density vs temperature for 100 × 500-μm device.
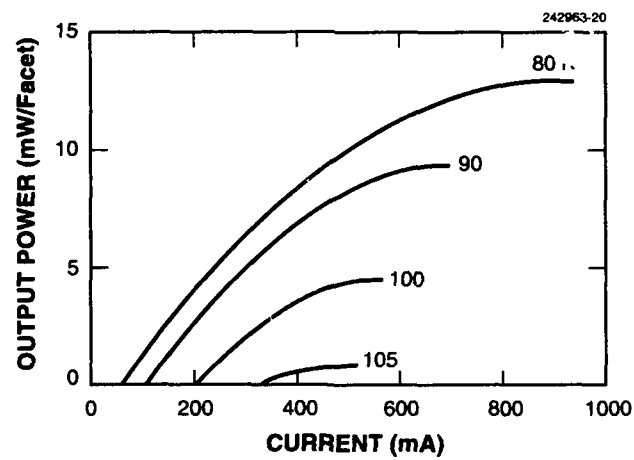
Figure 3-2. CW light output vs current for 60 × 500-μm device at several heatsink temperatures.

Figure 3-2 shows the CW output power vs current curves for a 60-μm-wide device at heatsink temperatures from 80 to 105 K. These curves were obtained by measuring the output with an InSb detector in the linear regime and calibrating it with a thermopile detector. The maximum power at 80 K is 12.5 mW/facet, with an initial differential quantum efficiency of 19% from both facets. Another device 100 μm wide was coated to have high (~ 90%) and low (~ 10%) reflectivity on the back and front facet, respectively. The maximum power from this device at 70 and 80 K is 30 and 24 mW, respectively. The output power from these lasers has been very stable during a few hours of measurement as well as a few temperature cycles.

The emission spectrum shows multiple longitudinal modes that are 3.9 nm apart. Figure 3-3 plots the peak emission wavelength under pulsed operation as a function of temperature. Between 80 and 130 K the wavelength increases with temperature at a rate of 1.5 nm/K, which is somewhat less than ~ 2 nm/K expected from the bandgap shift with temperature. The smaller rate probably results from bandfilling because of a very low T_0. The effect of bandfilling is much more pronounced at temperatures > 140 K.

H. K. Choi   W. L. McGilvary
G. W. Turner   J. V. Pantano
M. K. Connors   D. R. Calawa
J. W. Chludzinski
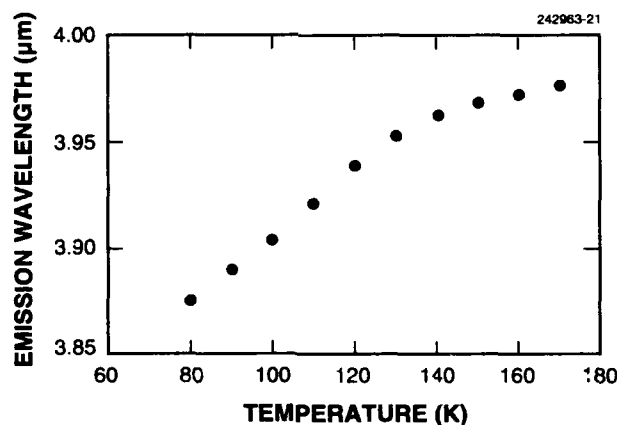
Figure 3-3. Pulsed emission wavelength of devices at temperatures from 80 to 170 K.

3.2 GROWTH OF GaSb FROM TRIETHYLGALLIUM AND TRIMETHYLANTIMONY

Previously, we reported the growth of GaSb by organometallic vapor phase epitaxy (OMVPE) from trimethylgallium (TMGa) and trimethylantimony (TMSb) [5]. The growth rate increased with substrate temperature over the range investigated from 560 to 640°C, and unintentionally doped GaSb layers were p-type with a low carrier concentration of 1.1×10^{16} cm^{-3} and high hole mobility of 3.8×10^3 cm^2/V s measured at 77 K. In the present study, improvements in the growth characteristics and electrical properties are reported for GaSb grown with triethylgallium (TEGa) and TMSb.

The GaSb epilayers were grown in a vertical rotating-disk OMVPE reactor operated at 0.2 atm. The carrier gas was H_2 at a flow rate of 10 slpm. The TEGa mole fraction ranged from 1 to 3×10^{-4}, while the TMSb mole fraction ranged from 1.9 to 7.2×10^{-4}, which resulted in a V/III ratio range between 0.7 and 2.4. The GaSb growth temperature was varied from 525 to 640°C. GaSb epilayers were grown on Te-doped GaSb substrates oriented 2° toward [110] or on semi-insulating GaAs substrates for electrical measurements.

Figure 3-4 shows the GaSb growth rate, normalized to the group III mole fraction, as a function of inverse temperature for layers grown from either TMGa and TMSb [5] or TEGa and TMSb. With TMGa as the group III source, growth is kinetically limited over the entire temperature range between 560 and 640°C. On the other hand, growth is mass transport limited for TEGa, since the normalized growth rate is nearly constant at about 2.7 Å/s for the temperature range between 525 and 625°C. These results are consistent with data showing that the decomposition temperature for TEGa is about 100°C lower than for TMGa [6]. Although the normalized growth rate is lower for TEGa than TMGa, growth with TEGa would be advantageous over TMGa since variations in substrate temperature will have a negligible effect on the growth rate. In addition, the composition of ternary or quaternary GaSb-based alloys will be less sensitive to substrate temperature nonuniformity and temperature fluctuations.

The surface morphology of GaSb layers is sensitive to V/III ratio. For a minimum V/III ratio, GaSb epilayers were mirror; otherwise gallium droplets were observed. The minimum V/III ratio for obtaining stoichiometric GaSb with mirror morphology on GaSb substrates is shown as a function of growth temperature by the solid line in Figure 3-5. For temperatures > 600°C the V/III ratio required for mirror morphology is 0.9 or greater, while for temperatures < 600°C the minimum V/III ratio increases with decreasing temperature and for a growth temperature of 525°C is 1.9. Since the growth rate, which is determined by the extent of TEGa decomposition, is constant between 525 and 625°C, these results suggest that the thermal decomposition of TMSb is incomplete below 600°C in our reactor. The reported thermal decomposition temperature of TMSb [7] is ~ 550°C. For GaSb growth on GaAs substrates the minimum V/III ratio was typically 0.1–0.2 higher than that required for growth on GaSb substrates.

Electrical properties of the epitaxial GaSb were measured on layers grown on GaAs substrates. Since the electrical properties of mismatched epilayers can be dominated by the characteristics near the substrate/epilayer interface, the GaSb layers were grown at least 3 μm thick for Hall measurements. The effect of growth temperature on the electrical properties measured at 77 K is shown in Figure 3-6 for epilayers grown either with TEGa or TMGa [5] and with a sufficient V/III ratio to obtain stoichiometric GaSb. The layers were p-type for both TEGa and TMGa growth. A reduction in hole concentration and increase in hole mobility are observed in all cases for growth with TEGa compared to TMGa in the

30
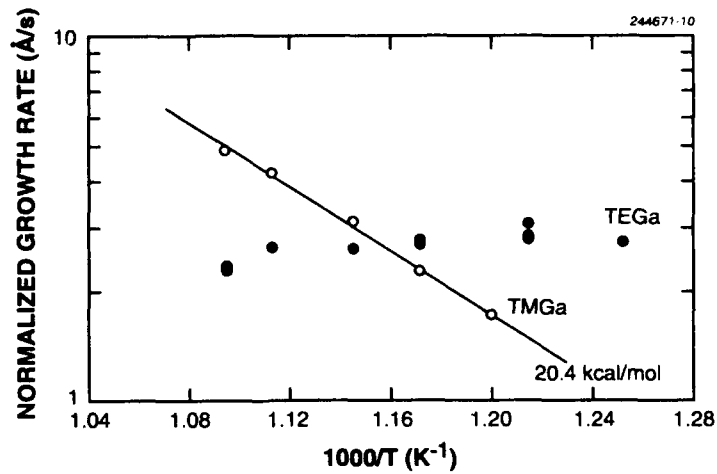
Figure 3-4. GaSb growth rate, normalized to the group III mole fraction, vs inverse growth temperature for TMGa with TMSb, and TEGa with TMSb.
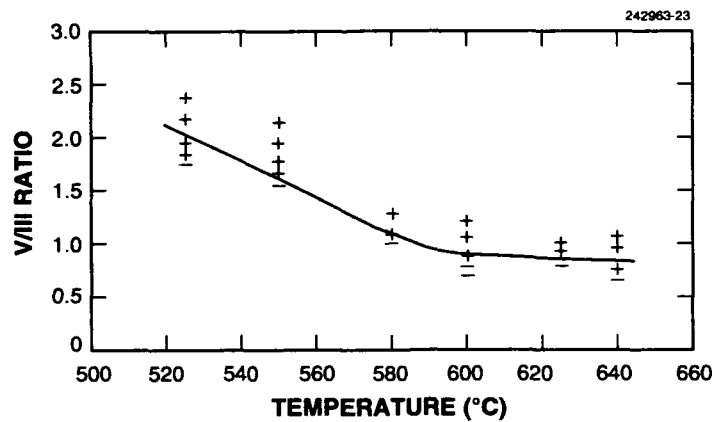
Figure 3-5. Solid line indicates minimum V/III ratio vs growth temperature for optimum surface morphology of GaSb layers grown with TEGa and TMSb. Plus (+) data points indicate stoichiometric and minus (−) points Ga-rich epilayers.

31
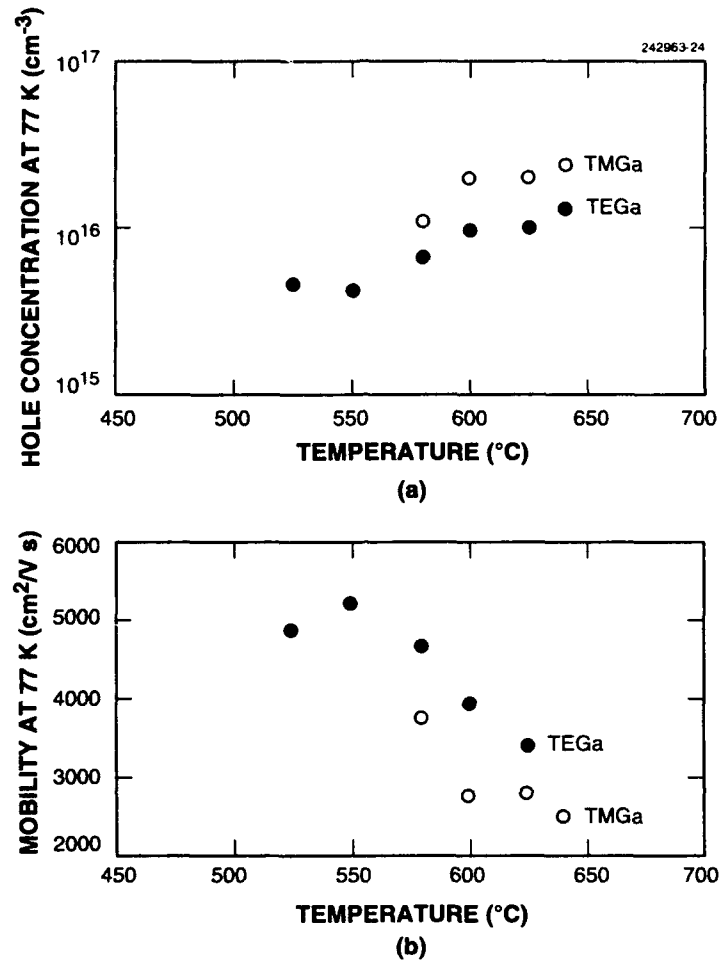
Figure 3-6. (a) Hole concentration at 77 K and (b) mobility at 77 K, both as a function of growth temperature for TEGa with TMSb, and TMGa with TMSb.

temperature range between 580 and 640°C. Further reduction in hole concentration and increase in mobility are obtained for growth with TEGa at the lower growth temperatures of 525 and 550°C. The lowest hole concentration was 3.4×10^{15} cm^{-3} with corresponding hole mobility of 5.4×10^3 cm^2/V s, which was obtained for layers grown at 550°C and V/III = 2.0. These values are better than those previously reported for any GaSb grown by OMVPE.

C. A. Wang
J. H. Reinold

32

REFERENCES

1. H. K. Choi and S. J. Eglash, *Appl. Phys. Lett.* **61**, 1154 (1992).

2. H. K. Choi, G. W. Turner, and S. J. Eglash, *IEEE Photon. Technol. Lett.* **6**, 7 (1994).

3. H. K. Choi, S. J. Eglash, and G. W. Turner, *Appl. Phys. Lett.* **64**, 2474 (1994).

4. S. J. Eglash and H. K. Choi, *Appl. Phys. Lett.* **64**, 833 (1994).

5. Solid State Research Report, Lincoln Laboratory, MIT, 1993:4, p. 18.

6. G. B. Stringfellow, *Organometallic Vapor-Phase Epitaxy: Theory and Practice* (Academic, New York, 1989).

7. C. A. Larsen, R. W. Gedridge, Jr., S. H. Li, and G. G. Stringfellow, *Proc. Mater. Res. Soc. Symp.* **204**, 129 (1991).

4. SUBMICROMETER TECHNOLOGY

4.1 SCALED DEVICES FOR HIGH-DENSITY MEMORIES

A scalable vertical device structure and voltage programmable link (VPL) are being developed [1] for fabricating an ultradense programmable read-only memory (PROM). The goal is to construct solid-state PROM integrated circuits with storage capacity comparable to a compact disk read-only memory but with much higher bit density and a much faster access time. Implementing this much storage on a chip of 2-cm^2 area will require a memory cell pitch of 0.2 μm. This necessitates the use of aggressive lithographic techniques and an efficient memory cell structure.

The vertical metal-oxide semiconductor field-effect transistor (MOSFET) memory cell, seen in Figure 4-1(a), is a very compact topology since the source contact, self-aligned drain contact, channel, and VPL are stacked. This three-dimensional device can be readily utilized in a memory array, as seen in Figure 4-1(b). The substrate provides the common source connection. The VPLs are formed at the tops of the devices and are tied to the bit lines. The word lines are connected to the gates of the transistors along a row within the array. In this configuration the channel length is determined by the height of the structure so that the memory cell pitch and gate length can be scaled independently. Thus, it should be possible to achieve long-channel device performance in a very dense array.

The PROM can be fabricated with either n- or p-channel devices. The n-channel transistors have superior mobility and hence superior switching speed, but the fabrication of p-channel devices is less complex. When p-channel transistors are used the VPL can be directly formed on the p^+ drain, and the devices are inherently less prone to anomalous electrical characteristics caused by the so-called floating-body effect [2]. We have experimented with both types of devices.

Fabricating this PROM array requires four lithographic steps. The first mask defines the transistor locations, which are formed using reactive ion etching (RIE) with $HeCl_2$ chemistry. In the current process, i-line lithography is used to define the 0.6-μm-diam transistors that are etched 1.5 μm into the substrate. An alternative HBr etch chemistry is being developed to scale the process to smaller dimensions. In recent tests, scanning electron-beam lithography has been used to define test structures < 0.1 μm in diameter that have been successfully etched to a 1-μm depth. After etching, a wet sacrificial oxide is grown and stripped to remove any damage along the device sidewall that may have been caused by the RIE. The final 20-nm-thick gate oxide is then grown. A 200-nm-thick layer of 580°C amorphous silicon (a-Si), which will form the gates (word line), is deposited using low-pressure chemical vapor deposition (LPCVD). After the second mask, in which the photoresist is patterned, O_2 RIE is used to remove the photoresist from the tops of the silicon pillars prior to the word line etch. This allows the a-Si to be removed from the tops of the pillars and recessed down the sidewalls during the Cl_2-based plasma etch. At this point angled and rotated ion implantation is used to form the lightly doped drain structure at the top of the device and to dope the a-Si gate. A short thermal oxidation activates the implant and crystallizes the polysilicon gate. Figure 4-2 illustrates the device at this stage.

35

242963-25

(a)

GATE OXIDE

VOLTAGE PROGRAMMABLE LINK

n-TYPE Si

p-TYPE Si

GATE

n-TYPE Si

(b)

VOLTAGE PROGRAMMABLE LINK

WORD LINE

WORD LINE

WORD LINE

BIT LINE

BIT LINE

BIT LINE
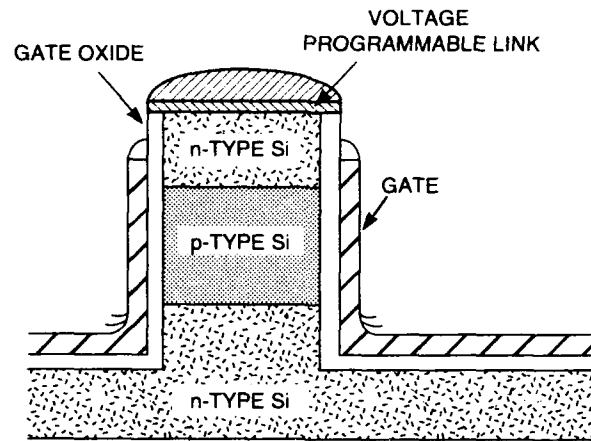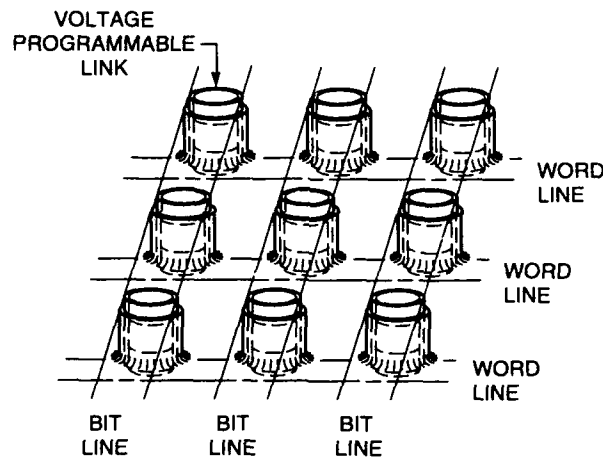
Figure 4-1. (a) Cross section of n-channel vertical metal-oxide semiconductor field-effect transistor (MOSFET) and voltage programmable link. The device is cylindrical, the drain is located at the top, and the current flow is from top to bottom. The gate encircles the device, and the substrate forms the source connection. (b) Schematic representation of device in (a) used in a programmable read-only array.

242963-26

1 μm
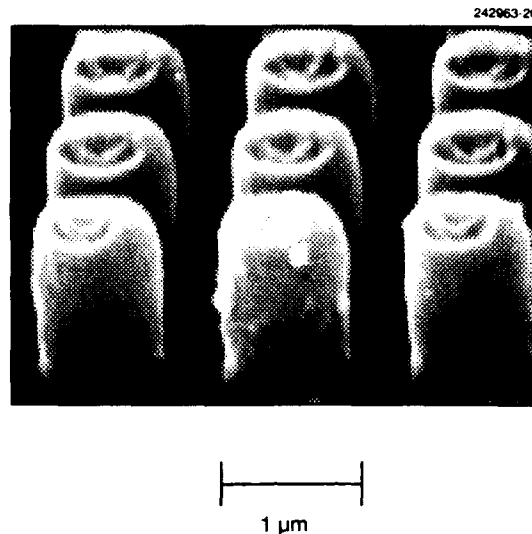
Figure 4-2. Scanning electron micrograph of partially fabricated vertical MOSFETs. At this point the cylindrical structure has been defined, and the polysilicon gate has been deposited and patterned. In the next step a tetraethylorthosilicate oxide is deposited to fill in the trenches between devices.

Next, a 2-μm-thick layer of LPCVD tetraethylorthosilicate oxide is deposited to fill in the spaces between the devices, but this layer is conformal and results in an uneven top surface. A chemical mechanical polishing process is used to globally planarize the surface and remove the oxide down to the tops of the silicon pillars forming the self-aligned drain contacts. The n-channel VPL formation begins with a self-aligned titanium silicide layer, which reduces the drain contact resistance (p-channel devices do not require the silicide layer). Then, a dielectric stack consisting of 5-nm-thick layers of silicon nitride, silicon dioxide, and silicon nitride is in situ deposited using plasma-enhanced chemical vapor deposition. The third mask is used to define conventional contact cuts to the polysilicon word lines at the perimeter of the array. The bit line metal consists of a three-layer stack of in situ sputter-deposited aluminum silicon (20 nm), titanium (20 nm), and aluminum silicon (600 nm). The bit lines are patterned using the fourth mask and etched with Cl_2-based RIE.

The smallest transistor arrays fabricated, using conventional i-line photolithography, utilize 0.6-μm-diam devices on a 1.6-μm pitch. Typical n-channel device characteristics are shown in Figure 4-3. These measurements indicate that the use of a lightly doped source and a lightly doped drain has suppressed the floating-body effect. The transistors exhibit a drain-to-source breakdown > 12 V and an off-state leakage current < 50 pA at V_{DS} = 5 V. These device characteristics are suitable for the fabrication of large programmable memory arrays.

37
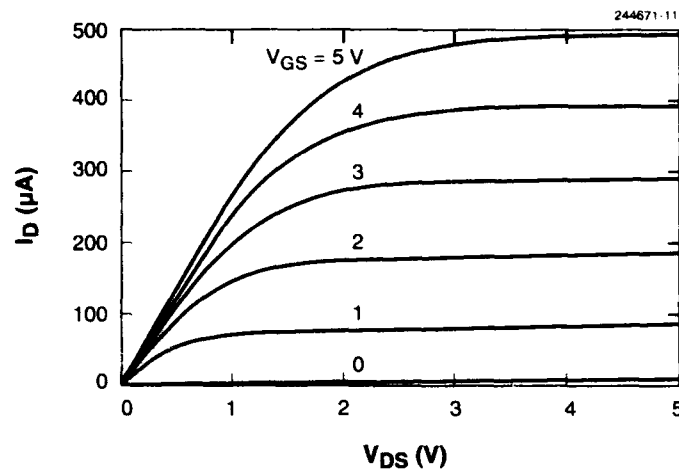
Figure 4-3. Measured current vs voltage characteristics for the 0.6-μm-diam n-channel vertical MOSFETs.

The VPL is a normally open write-once structure. It remains nonconducting until voltages in excess of the programming threshold are applied. After programming, the VPL becomes permanently conducting. Arrays of VPLs have been fabricated on p^+ silicon structures to assess their programming characteristics. Figure 4-4 is a histogram of the measured programming thresholds for 0.6-μm-diam VPLs. The distribution is centered at ~ 9.5 V with a standard deviation of ~ 1 V.

Current efforts involve investigating the scaling limits for the vertical FET structure. We have recently fabricated 0.3-μm-diam p-channel MOSFETs with the i-line stepper using chromeless phase-shift mask techniques. The devices were functional, but they exhibited a low breakdown voltage (~ 6 V) due to a thermal processing error. This should be remedied in the current device run.

C. L. Keast   C. L. Dennis
J. E. Murguia   M. W. Horn

242963-26
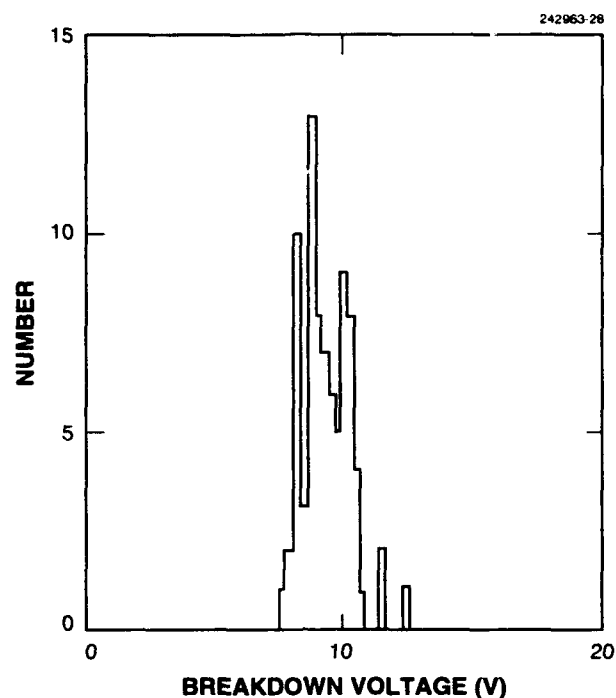
Figure 4-4. Breakdown voltage histogram for the voltage programmable link structure formed on 0.6-μm-diam p+ silicon structures.

4.2 FIELD EMISSION FROM CESIUM-TREATED DIAMOND SURFACES

Under certain conditions, diamond exhibits negative electron affinity (NEA), that is, the minimum energy of electrons in the conduction band can be larger than the minimum energy of electrons in vacuum [3]–[5]. This property should be useful for the fabrication of robust field-emission cold cathodes that operate at very low applied fields, but constructing such a cathode has proven to be challenging because electron emission varies with crystal orientation, surface treatment, and doping. The (111)-oriented diamond surface exhibits NEA, while under the same conditions the (100)-oriented surface has a positive electron affinity [5]. The presence of adsorbed atoms further modifies the electron affinity, but unlike other NEA materials [6]–[8], diamond will tolerate exposure to O_2 and organic solvents [3]. Doping can also have a major impact on emission properties, and the lack of readily available n-type diamond has impeded the development of diamond cathodes.

This report describes a surface treatment with cesium, a low work function material, that enhances the NEA property of diamond. It is speculated that under these conditions the electrons can be emitted from impurity bands in the bandgap rather than from just the conduction band. Such an increase in the NEA property reduces the need for n-type diamond for the fabrication of cold cathodes.

39

For these experiments both high-pressure synthetic diamond and diamond layers grown homoepitaxially on natural diamond were used. The homoepitaxial diamond was obtained using a chemical vapor deposition (CVD) technique in a hot-filament reactor. During growth $B(OCH_3)_3$ or LiCl was added to the growth environment to produce boron or lithium doping, respectively. The boron-doped layers were consistently p-type, but the Li-doped layers varied from sample to sample between n- and p-type as determined by both the Seebeck effect and Hall measurements. The high-pressure synthetic diamond was obtained from commercial sources and is type Ib, that is, it contains primarily nitrogen plus some boron impurities. The nitrogen is substitutional, forming a deep donor ~ 1.7 eV below the conduction band.

Prior to testing, the diamonds were cleaned in a 150°C solution of H_2SO_4 and H_2O_2, rinsed in water and acetone, and plasma ashed in a gas mixture of 3% O_2 in He. After loading in an oil-free vacuum system, an additional in situ plasma discharge with ~ 1 Torr of either H_2 or O_2 was performed for 5 min to form a hydrogen- or oxygen-terminated surface, respectively. The sample was then heated to 200°C for at least 10 h at a vacuum pressure $< 1 \times 10^{-7}$ Torr.

Figure 4-5 shows a schematic diagram of the experimental setup used to measure emission. The anode consists of a 1-mm-diam molybdenum wire, ground flat on the active end above the sample. An external X-Y-Z manipulator is used to move the anode above the sample. Cesium was deposited from a resistively heated Cs getter, and the deposition was continued until the electron emission properties of the sample exhibited no substantial increase with additional cesium.

As expected, the addition of Cs to the sample surface causes a substantial increase in the emission current at a given electric field, as shown in Figures 4-6 and 4-7 for Li-doped diamond layers on natural diamond. However, Cs coatings are usually very sensitive to ambient conditions. In particular, for the sample in situ treated with a H_2 discharge, exposure to heat and O_2 counteracted the enhancement and the emission was reduced to values similar to those of the Cs-free sample, as seen in Figure 4 ' In contrast, when the sample was cleaned and in situ treated with an O_2 discharge, the enhancem in emission due to Cs did not degrade and in some cases actually improved with heat treatment and reexposure to O_2, as shown in Figure 4-7. The type Ib synthetic diamonds exhibit similar heat- and O_2-stable emission enhancement after Cs treatment. Boron-doped homoepitaxial samples grown by CVD also exhibit emission enhancement with Cs treatment, but this enhancement is not stable with heat and O_2 treatment, even with in situ O_2 discharge, as seen in Figure 4-8.

244165-2

MOLYBDENUM →
ANODE
100 μm   A
DIAMOND CATHODE
CATHODE SUPPORT
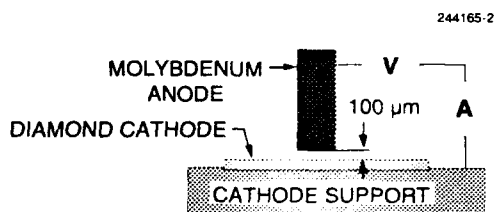
Figure 4-5. Diagram of experimental setup used for measurement of electron emission.
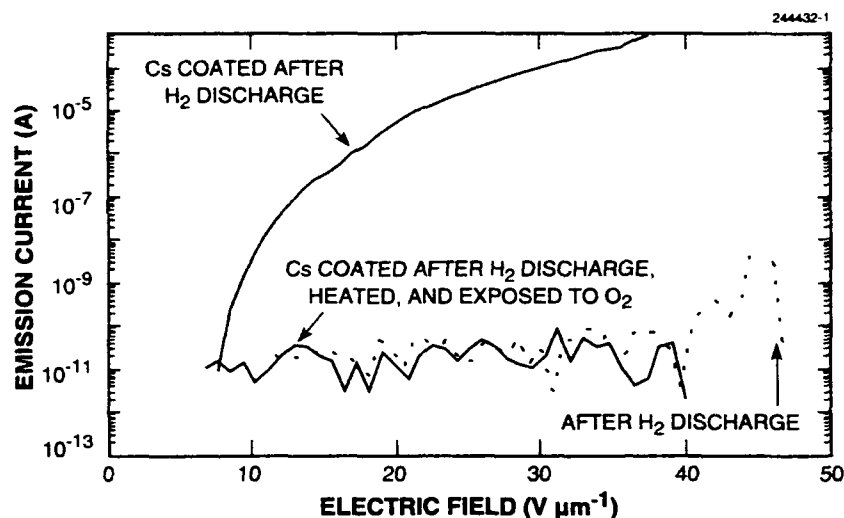
Figure 4-6. Electron emission as function of electric field for Li-doped homoepitaxial diamond layers that had been previously exposed to a H_2 discharge. Although the deposition of Cs increased the electron emission, heat and exposure to O_2 reduced the emission to its previous value.
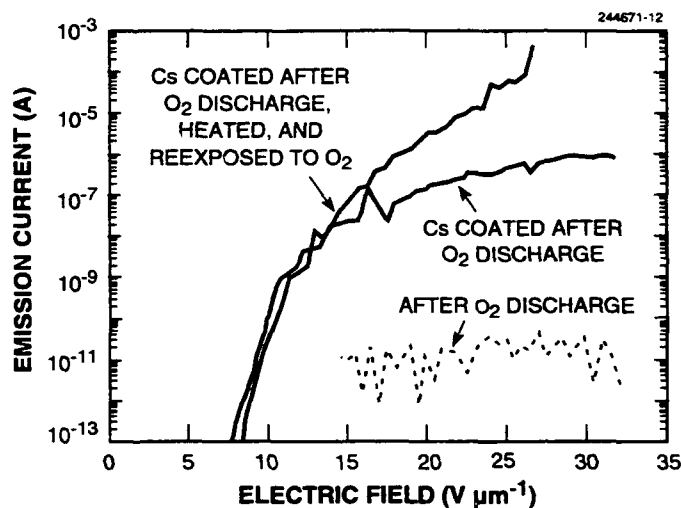
Figure 4-7. Electron emission as function of electric field for Li-doped homoepitaxial diamond layers that had been previously exposed to O_2 discharge. The deposition of Cs increased the electron emission, but the effect is more robust than in Figure 4-6. Heat and exposure $\cdots O_2$ do not degrade and in this case may actually improve the emission somewhat.

41
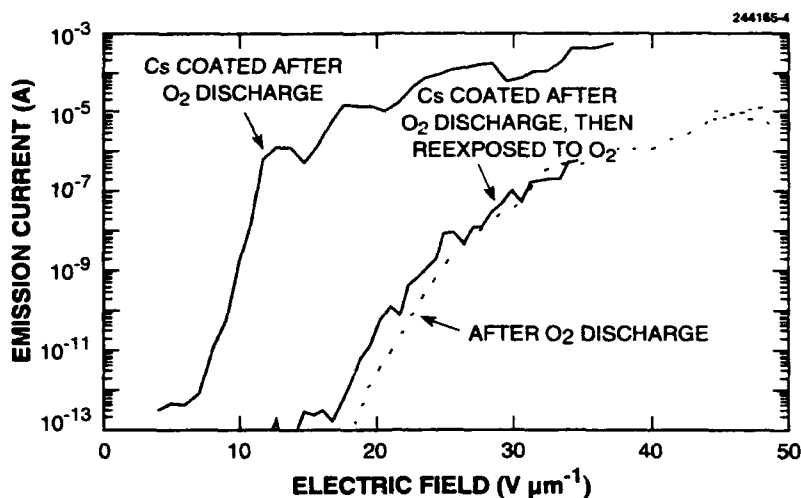
Figure 4-8. Electron emission as function of electric field for B-doped homoepitaxial diamond layers that had been previously exposed to O_2 discharge. Although the deposition of Cs increased the electron emission, heat and exposure to O_2 reduced the emission to its previous value.

Our model explaining these results focuses on the surface chemistry of the diamond after treatment with H_2 or O_2 discharge. Exposure to the H_2 discharge saturates the diamond surface with H atoms. Since Cs is unreactive with most saturated hydrocarbons, it is not expected to react with the hydrogen-saturated diamond surface. So, although Cs may lower the work function of diamond, it will evaporate when heated or react when exposed to oxygen. On the other hand, a discharge formed from O_2 and the ubiquitous H_2O present in the chamber will produce an oxygen-saturated surface terminated with OH groups. Such functional groups will react with Cs to produce H_2 and form a Cs salt at the surface. This C-O-Cs salt is chemically similar to lye soap and can withstand exposure to heat and oxygen. Assuming the O-Cs bond has a dipole moment of 10 debye [9], then only 0.1% of the surface carbon atoms need be bound to an O-Cs atomic group to lower the work function of the surface by 1 V.

Doping also plays a role in the electron emission properties of diamond. The only source of electrons in boron-doped diamond is near the valence band, several electron volts below the vacuum energy level. So, even with a reduced work function a substantial energy barrier exists for electron emission. We believe that the enhanced emission observed with Cs-treated boron-doped diamond is caused by a metallic Cs layer. This coating is not very robust, and hence the observed emission degrades after exposure to air and heat. The energy levels associated with Li and P doping of diamond are unknown, but substitutional nitrogen is known to form an electron donor 1.7 eV below the conduction band. Assuming that the vacuum energy level is ~ 0.7 eV below the conduction band, the electrons available from the nitrogen donors are still 1 eV below the vacuum level. If the addition of O and Cs is used to increase the energy of the conduction band ~ 1 eV with reference to the vacuum energy level,

then the electrons from the nitrogen donors can be emitted into vacuum without a barrier. Under these conditions the emission current will be limited by the electric field inside the diamond that is required for hopping or tunneling of the electrons to the vacuum interface.

M. W. Geis
J. C. Twichell
J. Macaulay*

*Author not at Lincoln Laboratory.

REFERENCES

1. Solid State Research Report, Lincoln Laboratory, MIT, 1992:4, p. 25.

2. K. Kato, T. Wada, and K. Taniguchi, *IEEE Trans. Electron Devices* **ED-32**, 458 (1985).

3. F. J. Himpsel, J. A. Knapp, J. A. Van Vechten, and D. E. Eastman, *Phys. Rev. B* **20**, 624 (1979).

4. B. B. Pate, B. J. Waclawaski, P. M. Stefan, C. Binns, T. Ohta, M. H. Hecht, P. J. Jupiter, M. L. Shek, D. T. Pierce, N. Swanson, R. J. Celotta, I. Lindau, and W. E. Spicer, *Physica B* **117/118**, 783 (1983).

5. M. W. Geis, J. A . Gregory, and B. B. Pate, *IEEE Trans. Electron Devices* **38**, 619 (1991).

6. J. L. Dye, *Science* **247**, 663 (1990).

7. R. U. Martinelli and D. G. Fisher, *Proc. IEEE* **62**, 1339 (1974).

8. G. G. P. van Gorkom and A. M. E. Hoeberechts, *J. Vac. Sci. Technol. B* **4**, 108 (1986).

9. M. Karpus and R. N. Porter, *Atoms and Molecules* (W. A. Benjamin, New York, 1970), p. 263.

5. HIGH SPEED ELECTRONICS

5.1 FABRICATION AND PERFORMANCE OF $In_{0.53}Ga_{0.47}As/AlAs$ RESONANT TUNNELING DIODES GROWN ON GaAs SUBSTRATES

Resonant tunneling diodes (RTDs) have been fabricated in the pseudomorphic $In_{0.53}Ga_{0.47}As/AlAs$ material system on GaAs substrates. The RTDs have peak-to-valley current ratios (PVCRs) of ~ 9 and peak voltages of ~ 1 V at room temperature. These diodes can be combined monolithically with conventional GaAs three-terminal devices such as heterojunction bipolar transistors (HBTs), metal-semiconductor field-effect transistors, and pseudomorphic high electron mobility transistors to create high-speed switching devices, logic gates, and memory elements on GaAs substrates. Because of the high PVCR of the RTD, these circuits will have very low static power dissipation.

The RTD heterostructures were grown on semi-insulating GaAs using solid-source molecular beam epitaxy and the epitaxial layers shown schematically in Figure 5-1. The RTD structure consists of a 55-Å undoped $In_{0.53}Ga_{0.47}As$ quantum well with nominally 18-Å undoped pseudomorphic AlAs barriers, 400-Å lightly doped $In_{0.53}Ga_{0.47}As$ cladding layers, and heavily doped $In_{0.53}Ga_{0.47}As$ ohmic contact layers above and below the quantum well. The thicknesses of the InGaAs quantum well, the pseudomorphic AlAs barrier, and the lightly doped InGaAs buffer were chosen to provide a peak voltage of ≤ 1 V and a peak current density of ~ 2×10^4 A/cm^2. A buffer was inserted between the GaAs substrate and the RTD active layers that consisted of a 1500-Å-thick undoped low-temperature-grown (LTG) $In_xGa_{1-x}As$ layer with x graded from 15 to 53% and a 3000-Å undoped LTG $In_{0.53}Ga_{0.47}As$ layer.

246382-1

500 Å	InGaAs	1.3×10^{19} cm^{-3}
1000	InGaAs	2.0×10^{18}
400	InGaAs	2.0×10^{16}
18	AlAs	UNDOPED
55	InGaAs	UNDOPED
18	AlAs	UNDOPED
400	InGaAs	2.0×10^{16}
4000	InGaAs	1.0×10^{18}
4000	InGaAs	1.3×10^{19}
3000	LTG InGaAs	UNDOPED
~1500	GRADED LTG InGaAs	UNDOPED

GaAs SEMI-INSULATING SUBSTRATE

Figure 5-1. Schematic of epitaxial layers for growth of $In_{0.53}Ga_{0.47}As/AlAs$ resonant tunneling diode (RTD).

After growth, RTD mesas were fabricated by standard photolithography, ohmic-contact metalliza-tion, photoresist lift-off, and wet-etching steps. The current-voltage characteristics of an $In_{0.53}Ga_{0.47}$ As/AlAs RTD grown on a GaAs substrate are shown in Figure 5-2. This device has an active area of ~ 9 μm^2. When the top ohmic contact is biased negatively, the device has a PVCR of 9.3, a peak voltage of 1.0 V, and a peak current density of 1.7×10^4 A/cm^2. When the anode is biased positively, the device has a PVCR of 6.1, a peak voltage of 0.65 V, and a peak current density of 1.1×10^4 A/cm^2. The negative bias PVCR is 50% greater than any reported in RTDs made from the lattice-matched AlGaAs/GaAs or AlAs/GaAs material systems [1]. When compared to an identical RTD structure grown lattice matched on an InP substrate, these RTDs exhibit only a 20% reduction in PVCR with similar peak current and voltage.

The LTG $In_xGa_{1-x}As$ buffer layer was critical to producing high PVCRs. Other buffers such as superlattices and thick InGaAs layers produced inferior RTDs. The LTG buffer appears to serve two functions. First, it accommodates the large lattice mismatch (~ 4%) between the GaAs substrate and the $In_{0.53}Ga_{0.47}As$ RTD by the formation of misfit and threading dislocations. Second, it traps these dislo-cations and prevents their propagation into the RTD structure grown above it [2]. GaAs substrates with crystallographic orientations of both (100) and (100) 2° off toward (110) were used with little difference in the RTD characteristics. The off-axis RTD can be overgrown directly on HBTs and on other transistors produced by organometallic chemical vapor deposition.

K. B. Nichols   E. R. Brown
M. J. Manfra   O. B. McMahon
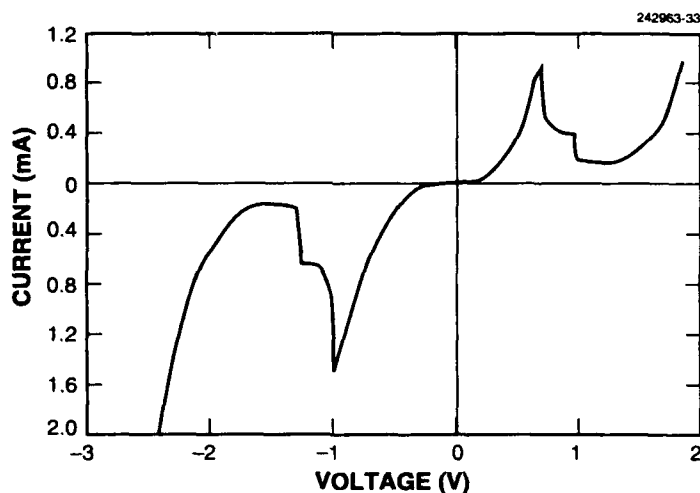
Figure 5-2. Current-voltage characteristics of $In_{0.53}Ga_{0.47}As$/AlAs RTD.

REFERENCES

1. V. K. Reddy, A. J. Tsao, and D. P. Neikirk, *Electron. Lett.* **26**, 1742 (1990).

2. D. E. Grider, S. E. Swirhun, D. H. Narum, A. I. Akinwande, T. E. Nohava, W. R. Stuart, P. Joslyn, and K. C. Hsieh, *J. Vac. Sci. Technol. B* **8**, 301 (1990).

6. MICROELECTRONICS

6.1 CONTROL OF PLASTIC DEFORMATION IN HIGH-RESISTIVITY CCDs

Charge-coupled devices (CCDs) can act as excellent imagers for x-rays. However, to image x-rays in the kilo-electron-volt energy range, such as for the Advanced X-Ray Astrophysics Facility, requires active Si thicknesses on the order of tens of micrometers, and it is desirable that the Si be fully depleted to obtain the best spatial resolution. This, in turn, requires starting material with doping levels of $< 10^{13}$ cm^{-3}, which can only be met by using Si that is float-zone (FZ) grown. Unlike Si that is Czochralski (CZ) grown where the O atoms pin or retard the motion of dislocations, FZ Si does not contain a supersaturation of oxygen in the Si lattice. Consequently, FZ Si is more susceptible to plastic deformation at temperatures of 600–700°C or higher because of the easy motion and multiplication of dislocations during the application of stress. These dislocations manifest themselves in the operation of the CCD as an increase in the charge-transfer inefficiency (CTI) of the device and as horizontal and vertical areas of higher than normal dark current. The present requirements for operation of a CCD for x-ray imaging applications are very severe and are difficult to achieve even in CZ material. These requirements include a CTI of $\leq 3 \times 10^{-6}$ and dark currents of < 1 electron/pixel·second, so the presence of dislocations cannot be tolerated.

The fabrication of CCD imagers using our standard process on CZ material or epitaxial Si on CZ substrates gives excellent results [1], with no evidence of dislocation-induced defects. However, when this same process is used to fabricate devices on high-resistivity FZ material, many dislocations are introduced, as shown in the dark current pattern of Figure 6-1. The streaks indicate the path taken by a set of dislocations as they moved through the crystal. The length of the streaks can be some tens of pixels, although not every pixel along the streak is a source of high dark current. The individual dislocations are also revealed by a preferential etching technique [2] and are seen in Figure 6-2 as a line of pits cutting across the channels of a CCD from a lot with the same processing and a similar degree of slip (the sausage-shaped figures are etching artifacts in the channel-stop region). For these devices the average CTI was on the order of 20×10^{-6}.

The origin of plastic deformation in Si can be attributed to stresses induced at high temperatures due to, for instance, thermal gradients in the wafer or the presence of intrinsic stresses in overlying layers [3]. Stresses due to thermal gradients or to the wafers lagging the temperature of the furnaces were reduced by introducing wafer-handling equipment within the furnaces that had lower heat capacity and high thermal conductivity. Careful attention was also paid to the details of introducing and withdrawing wafers from the furnace and to the change of furnace temperature with time. Use of the preferential etchant on test wafers at various stages during the fabrication process indicated that the structure and configuration of thin layers incorporated in the fabrication of the CCDs (silicon dioxide, silicon nitride, and polysilicon) had to be altered to eliminate the appearance of dislocations in the dark current map of finished devices. The results of the improved procedure are shown in the dark current pattern of Figure 6-3, where it is evident that no dislocations are present; the CTI of these devices is measured at $\sim 1 \times 10^{-6}$. Such a device can meet the present specifications of the most stringent CCD applications.

J. A. Gregory
R. W. Mountain

Figure 6-1. Dark current image of charge-coupled device (CCD) chip with dislocatic.i slip lines exhibited by bright vertical and horizontal streaks. Vertical dark line is due to unrelated defect.
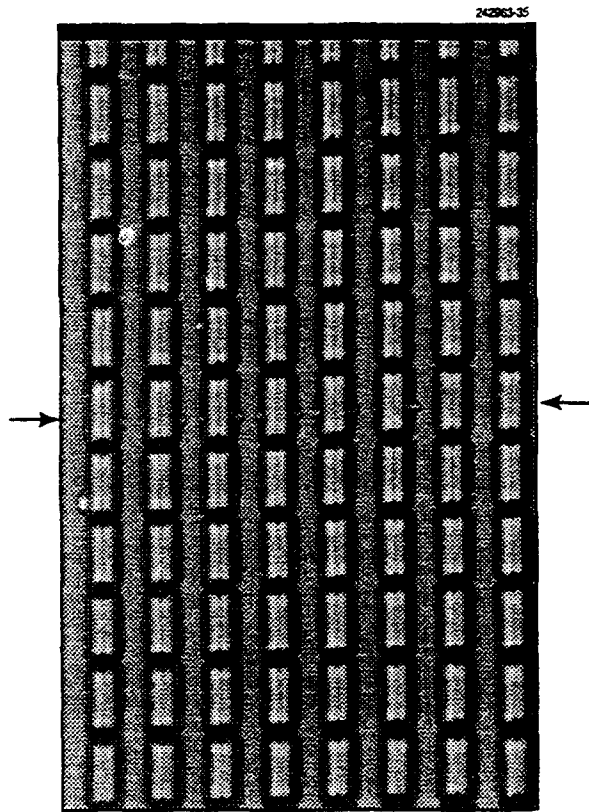
Figure 6-2. Slip line with dislocation etch pits revealed by preferential etchant (400×).

242963-34L
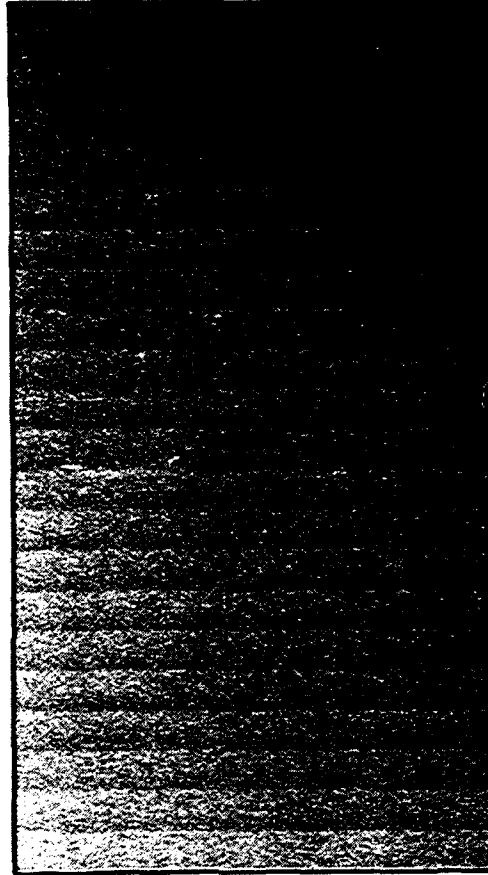
Figure 6-3. Dark current image of CCD chip without dislocation slip lines.

REFERENCES

1. B. E. Burke, J. A. Gregory, R. W. Mountain, J. C. M. Huang, M. J. Cooper, and V. S. Dolat, *Proc. SPIE* **1693**, 86 (1992).

2. *Annual Book of ASTM Standards* (American Society for Testing and Materials, Philadelphia, 1983), 10.05 F-47, p. 81.

3. S. M. Hu, *J. Appl. Phys.* **70**, R53 (1991).

7. ANALOG DEVICE TECHNOLOGY

7.1 SUPERCONDUCTIVE SPREAD-SPECTRUM MODEM OPERATING AT 2 GIGACHIPS PER SECOND

Communications demands for both civilian and military purposes are at the brink of explosive growth. Within orbital and terrestrial grids, there is a need for wireless, multiple-access communication networks that can support asynchronous data transfer rates in the range of 5–500 megabits per second per channel, orders of magnitude beyond what is available from current technology.

Possible approaches for implementing multiple-access communications channels include time hopping, frequency hopping, and direct-sequence spread-spectrum encoding. The direct-sequence approach, which we are developing, turns each bit of data into a sequence of "chips" in a spreading code. For a 1 bit, the code is transmitted; for a 0 bit, the negation of the code is sent. The bandwidth of the transmission (the rate at which chips are sent) is expanded over the real data rate by a factor equal to the length of the code. For example, if one were to use the seven-bit pseudonoise sequence 0110100 as the code to send the data stream 1110100, the resulting chip stream would be

$$
\overbrace{0110100}^{1}\ \overbrace{0110100}^{1}\ \overbrace{0110100}^{1}\ \overbrace{1001011}^{0}\ \overbrace{0110100}^{1}\ \overbrace{1001011}^{0}\ \overbrace{1001011}^{0}\ . \tag{7.1}
$$

The direct-sequence approach is the most demanding in terms of signal-processing algorithms and hardware but offers significant advantages. For DoD applications, it provides antijam capability, protection of emitter location for network nodes, and the lowest probability of intercept. For both civilian and military applications it affords the maximum reuse of bandwidth within an antenna beam, the convenience of sector (or omni-) broadcast antennas, and high resistance to multipath and fading.

The modem concept is illustrated in the block diagram of Figure 7-1. Superconductive electronics promises to achieve the desired leap in signal processor performance, since the intrinsic digital switching speed is in the range of hundreds of gigahertz. At the same time, our superconductive fabrication technology leverages developments in the semiconductor industry by using the same circuit design and layout tools and by employing a planarized process that can be fabricated on a silicon line. This immediately enhances yield for high-performance large-scale integrated circuits and opens the possibility of future cost-efficient foundry services. In this report, we discuss architectural and operational issues related to the modem.

The most challenging component in the modem system is the programmable binary-analog matched filter. A block diagram showing its architecture is presented in Figure 7-2. At the heart of the circuit is an analog data register, composed of an array of analog track-and-hold (T/H) circuits that together store at any given time the most recent N samples of the received analog signal. In each chipping interval of the spreading code, the oldest sample is replaced by a new sample. The analog signal is applied to all of the T/H cells, while the digital shift register, labeled sampling control register (SCR), circulates a single 1 that determines which T/H cell takes the new sample.

55
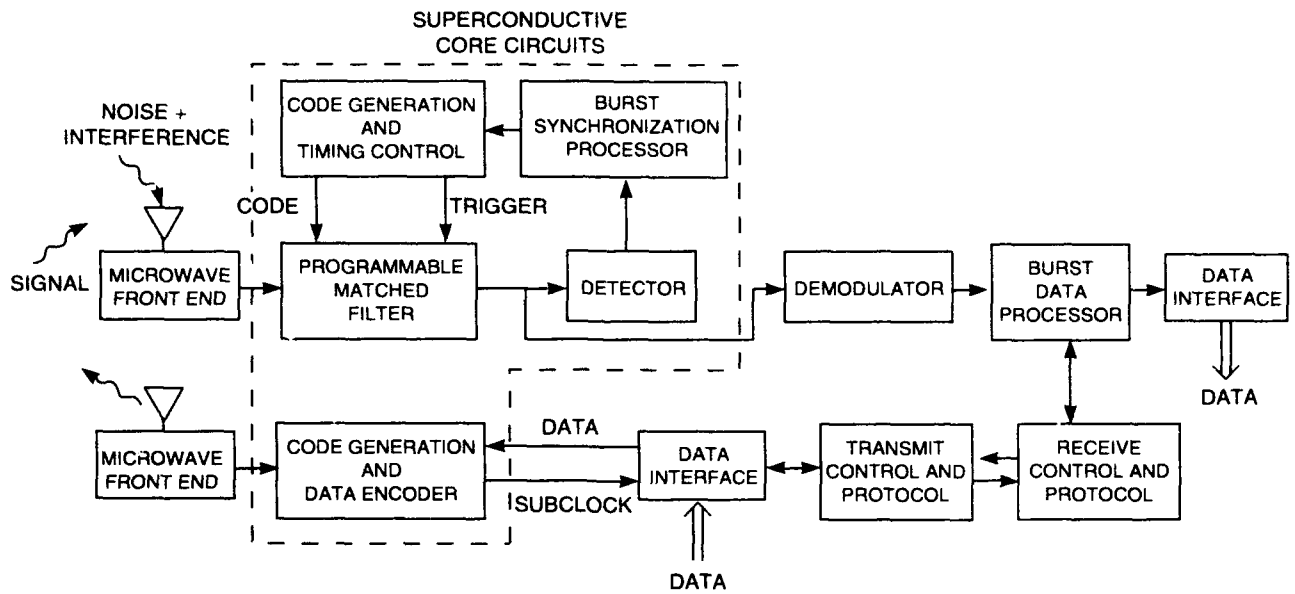
Figure 7-1. Block diagram of the spread-spectrum modem concept.
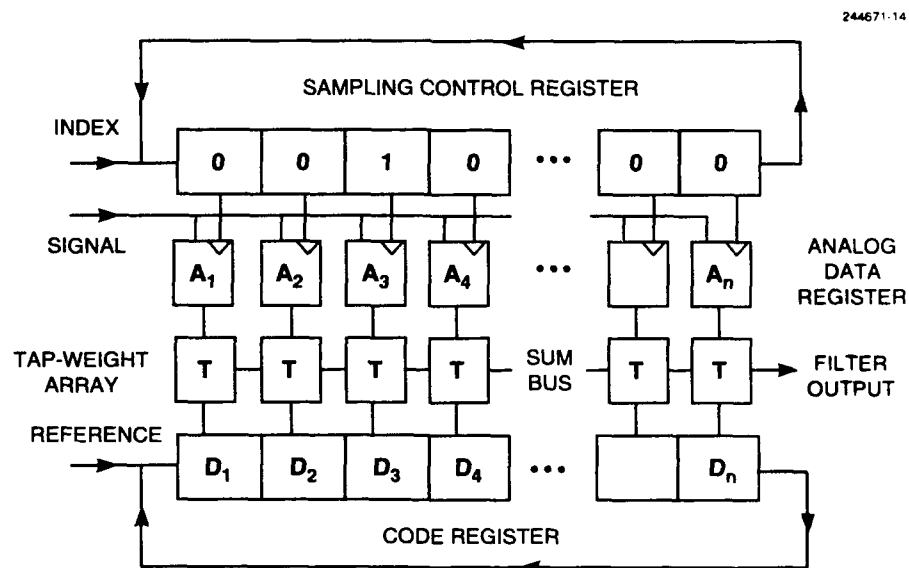
Figure 7-2. Architectural block diagram of high-speed programmable filter.

56

A second digital shift register, labeled code register, stores the values of the binary code that was used by the transmitter to encode the signal. At each stage of the filter, the analog output from the T/H cell and the binary value from the code register are multiplied in a tap-weight circuit. The outputs of all the taps are summed to provide the filter output, which is the correlation of the reference pattern with the signal pattern at that clock cycle.

The superconductive matched filter differs architecturally in one significant way from the transversal filter implementations we have developed in the past using other technologies, such as surface-acoustic-wave devices and charge-coupled devices. In those technologies the analog signal can be transported easily and accurately and is moved past a spatially fixed digital reference. Superconductive electronics does not support accurate resampling of an analog signal sample. However, it can hold an analog sample in place indefinitely in the form of a persistent current flowing in a superconducting loop. Superconductive electronics also provides very fast, low-power digital shift registers. Our filter architecture takes advantage of the relativity of motion and interchanges the way the analog and digital signals are handled. The analog samples remain in place while the digital reference code moves past them at the chipping rate, as seen in Figure 7-3.

The filter can be operated in two modes depending on whether the timing of the incoming signal is known or not. When a new signal is acquired, the delay between the signal and the code is not known and must be determined by the modem. This function, which must be performed very quickly, is termed burst synchronization. It requires the generation of the complete correlation function by the matched filter so that the time of the correlation peak can be determined.

The response of a seven-stage filter to a noise-free signal as given by sequence (7.1) is illustrated in Figure 7-3. Since repeating pseudonoise codes have optimal peak-to-sidelobe characteristics, they can serve well as a data packet header for synchronization acquisition. The bit pattern 1110100 is, thus, taken to comprise a header of 111 and initial data of 0100. We will assume for this example that the received signal is delayed by two chip clock pulses relative to the reference code, so that it starts with two extra 0 chips as follows:

$$00 \; \overbrace{0110100}^{1} \; \overbrace{0110100}^{1} \; \overbrace{0110100}^{1} \; \overbrace{1001011}^{0} \; \overbrace{0110100}^{1} \; \overbrace{1001011}^{0} \; \overbrace{1001011}^{0} \quad . \tag{7.2}$$

Note that a 0 represents a negative amplitude at baseband or a 180° phase shift in a carrier.

The upper block in Figure 7-3 shows the contents of the filter circuits after seven clock pulses. At this point the filter has been filled with the first seven chips of the incoming signal, and the reference code is aligned in the code register. Note that the 1 in the SCR always points to the end of the reference code. Because of the two-chip delay in the signal, the analog register contains a replica of the code rotated two stages to the right. Since 0 values in the analog and code registers represent analog values of –1, the outputs of the tap-weight circuits are +1 when the two input signals are the same (both 0 or both 1) and –1 when they are different. The values are designated in the figure by their signs alone. The sum of the tap weights, which is the filter output, is –1.

SCR	0	0	0	0	0	0	1	Tstep = 7
ANALOG	0	0	0	1	1	0	1	
CODE	0	1	1	0	1	0	0	
TAP	+	–	–	–	+	+	–	OUT = –1
SCR	1	0	0	0	0	0	0	Tstep = 8
ANALOG	0	0	0	1	1	0	1	
CODE	0	0	1	1	0	1	0	
TAP	+	+	–	+	–	–	–	OUT = –1
SCR	0	1	0	0	0	0	0	Tstep = 9
ANALOG	0	0	0	1	1	0	1	
CODE	0	0	0	1	1	0	1	
TAP	+	+	+	+	+	+	+	OUT = +7
SCR	0	0	1	0	0	0	0	Tstep = 10
ANALOG	0	0	0	1	1	0	1	
CODE	1	0	0	0	1	1	0	
TAP	–	+	+	–	+	–	–	OUT = –1
SCR	0	1	0	0	0	0	0	Tstep = 30
ANALOG	1	1	1	0	0	1	0	
CODE	0	0	0	1	1	0	1	
TAP	–	–	–	–	–	–	–	OUT = –7

Figure 7-3. Illustration of operation of matched filter when generating full correlation function for a noise-free packet header containing all 1 bits encoded by a pseudonoise sequence. The sampling control register (SCR) contains a single, circulating 1 which points both to the analog cell that takes the current sample and to the end of the circulating reference code. The outputs of the tap weight circuit (in the rows labeled TAP) are summed to arrive at the filter output.

At the next clock cycle the 1 in the SCR recirculates back to the beginning and causes the eighth sample of the input signal (a 0) to be stored in the first analog sampling cell. At the same time, the reference code is shifted one stage to the right, with the bit that exits from the right recirculating back to the beginning. Again the filter output is –1.

At the next clock cycle the 1 in the SCR shifts to the right and causes the ninth sample of the input signal (another 0) to be stored in the second analog sampling cell. The reference code is rotated one more stage to the right. The code is now aligned with the signal, and the filter output jumps to +7.

Because the input signal in this case is a repeating sequence, the contents of the analog register, in the absence of noise, do not change. As the code is rotated through the code register, it will line up with the input signal at a time that corresponds to the time delay of the signal with respect to the reference

code. The correlation output thus indicates the proper timing to use for detecting the encoded signal. The last panel in Figure 7-3 shows the situation after the 30th clock cycle, at which point the chips for a data bit of 0 have been stored in the analog register. The filter output is now −7.

Once the timing has been established, assuming it does not drift, it would no longer be necessary to rotate the reference code. The filter response is needed only at the correlation peak, which will be +7 for a 1 bit in the data stream and −7 for a 0 bit in the data stream. Outputs at other times would be ignored. This is the second mode in which the filter could be operated.

One further timing complication must be addressed by the burst synch processor. With a band-limited signal the amplitude will not make transitions between values of −1 and +1 instantaneously at the chip boundaries. As a result, the timing of the correlation peak must be determined on a finer scale than the chipping interval to make sure that it is centered on the data. In order to achieve an adequate signal-to-noise level, resolution to about one-quarter of the chipping interval is needed.

<div align="right">

J. P. Sage
R. W. Ralston

</div>

REPORT DOCUMENTATION PAGE

Public reporting burden for this collection of information is estimated to average 1 hour per response, including the time for reviewing instructions, searching existing data sources, gathering and maintaining the data needed, and completing and reviewing the collection of information. Send comments regarding this burden estimate or any other aspect of this collection of information, including suggestions for reducing this burden, to Washington Headquarters Services, Directorate for Information Operations and Reports, 1215 Jefferson Davis Highway, Suite 1204, Arlington, VA 22202-4302, and to the Office of Management and Budget, Paperwork Reduction Project (0704-0188), Washington, DC 20503

| 1. AGENCY USE ONLY (Leave blank) | 2. REPORT DATE
15 May 1994 | 3. REPORT TYPE AND DATES COVERED
Quarterly Technical Report, 1 February–30 April 1994 |
|---|---|---|

4. TITLE AND SUBTITLE

Solid State Research

5. FUNDING NUMBERS

C — F19628-90-C-0002
PE — 63250F
PR — 221

6. AUTHOR(S)

Alan L. McWhorter

7. PERFORMING ORGANIZATION NAME(S) AND ADDRESS(ES)

Lincoln Laboratory, MIT
P.O. Box 73
Lexington, MA 02173-9108

8. PERFORMING ORGANIZATION REPORT NUMBER

1994:2

9. SPONSORING/MONITORING AGENCY NAME(S) AND ADDRESS(ES)

HQ Air Force Materiel Command
AFMC/STSC
Wright-Patterson AFB, OH 45433-5001

10. SPONSORING/MONITORING AGENCY REPORT NUMBER

ESC-TR-94-093

11. SUPPLEMENTARY NOTES

None

12a. DISTRIBUTION/AVAILABILITY STATEMENT

Approved for public release; distribution is unlimited.

12b. DISTRIBUTION CODE

13. ABSTRACT (Maximum 200 words)

This report covers in detail the research work of the Solid State Division at Lincoln Laboratory for the period 1 February through 30 April 1994. The topics covered are Electrooptical Devices, Quantum Electronics, Materials Research, Submicrometer Technology, High Speed Electronics, Microelectronics, and Analog Device Technology. Funding is provided primarily by the Air Force, with additional support provided by the Army, ARPA, Navy, BMDO, NASA, and NIST.

14. SUBJECT TERMS

electrooptical devices	microelectronics	sum-frequency generation	diamond cathodes
quantum electronics	analog device technology	optical coatings	resonant tunneling diodes
materials research	lasers	epitaxial growth	charge-coupled devices
submicrometer technology	mass-transport microlenses	high-density memories	superconductive filters
high speed electronics			

15. NUMBER OF PAGES
84

16. PRICE CODE

| 17. SECURITY CLASSIFICATION OF REPORT
Unclassified | 18. SECURITY CLASSIFICATION OF THIS PAGE
Same as Report | 19. SECURITY CLASSIFICATION OF ABSTRACT
Same as Report | 20. LIMITATION OF ABSTRACT
Same as Report |
|---|---|---|---|